remote sensing

MDPI

Article

The Spatiotemporal Surface Velocity Variations and Analysis of the Amery Ice Shelf from 2000 to 2022, East Antarctica

Yuanyuan Ma [1,2], Zemin Wang [1,2], Baojun Zhang [1,2,*], Jiachun An [1,2], Hong Geng [3] and Fei Li [1,2]

[1] Chinese Antarctic Center of Surveying and Mapping, Wuhan University, Wuhan 430079, China; mayuanyuan123@whu.edu.cn (Y.M.); zmwang@whu.edu.cn (Z.W.); jcan@whu.edu.cn (J.A.); fli@whu.edu.cn (F.L.)
[2] Key Laboratory of Polar Environment Monitoring and Public Governance, Ministry of Education, Wuhan University, Wuhan 430079, China
[3] School of Resource and Environment Science, Wuhan University, Wuhan 430079, China; genghong@whu.edu.cn
* Correspondence: bjzhang@whu.edu.cn

Abstract: The surface velocity of the Amery Ice Shelf (AIS) is vital to assessing its stability and mass balance. Previous studies have shown that the AIS basin has a stable multi-year average surface velocity. However, spatiotemporal variations in the surface velocity of the AIS and the underlying physical mechanism remain poorly understood. This study combined offset tracking and DInSAR methods to extract the monthly surface velocity of the AIS and obtained the inter-annual surface velocity from the ITS_LIVE product. An uneven spatial distribution in inter-annual variation in the surface velocity was observed between 2000 and 2022, although the magnitude of variation was small at less than 20.5 m/yr. The increase and decrease in surface velocity on the eastern and western-central sides of the AIS, respectively, could be attributed to the change in the thickness of the AIS. There was clear seasonal variation in monthly average surface velocity at the eastern side of the AIS between 2017 and 2021, which could be attributed to variations in the area and thickness of fast-ice and also to variations in ocean temperature. This study suggested that changes in fast-ice and ocean temperature are the main factors driving spatiotemporal variation in the surface velocity of the AIS.

Keywords: Amery Ice Shelf; surface velocity variation; AIS thickness; fast-ice; ocean temperature

Citation: Ma, Y.; Wang, Z.; Zhang, B.; An, J.; Geng, H.; Li, F. The Spatiotemporal Surface Velocity Variations and Analysis of the Amery Ice Shelf from 2000 to 2022, East Antarctica. *Remote Sens.* **2024**, *16*, 3255. https://doi.org/10.3390/rs16173255

Academic Editor: Yi Luo

Received: 10 May 2024
Revised: 23 July 2024
Accepted: 2 August 2024
Published: 2 September 2024

1. Introduction

The Amery Ice Shelf (AIS) is the largest in the East Antarctic Ice Sheet and buttresses the Lambert Glacier Basin. The Lambert Glacier Basin is the fourth-largest basin in Antarctica, draining ~12.5% of the Antarctic Ice Sheet. Since the AIS drains only 2.5% of the East Antarctic coastline, it is a sensitive indicator of mass discharge of the East Antarctic Ice Sheet [1,2]. A report by the Intergovernmental Panel on Climate Change (IPCC, 2023) suggests that the warming climate results in enhanced surface and basal melting of ice shelves, which will drive increasing ice surface velocity [3]. Therefore, surface velocity is the most direct indicator of the movement of glaciers and ice sheets in Antarctica under the effects of global climate change [4]. Surface velocity measurements are important for understanding the motion of glaciers and ice sheets in Antarctica.

Satellite remote sensing can improve large-scale and high-resolution measurements of surface velocities, thereby providing the comprehensive observations required for modern scientific investigations of polar region ice movement [5–7]. Current measurements of ice movements mainly rely on synthetic aperture radar (SAR) and optical remote-sensing technology [8]. To derive ice motion using Sentinel-1 data, differential interferometric SAR (DInSAR) and offset tracking can be exploited. However, optical remote monitoring provides surface velocity with limited accuracy due to the impacts of sunshine and snow

clouds [9]. Monitoring surface velocities in recent decades has been improved by using SAR, which enables accurate large-scale detection of surface motion. For example, the Sentinel-1A and Sentinel-1B satellites can provide monthly measurements of surface velocity [10,11]. Many surface velocity datasets for the AIS have been released [6,12–14]. These datasets have been based on feature tracking or cross-correlation between optical images and DInSAR or offset tracking.

DInSAR has allowed the measurement of surface velocity at an unprecedented spatial resolution and precision of millimeter-to-centimeter levels [9]. However, the accuracy and temporal resolution of DInSAR data depend on the local environment and time between acquisitions. Consequently, ionospheric perturbations, tidal fluctuations, atmospheric effects, and fast-ice motion limit the accuracy of DInSAR methods [15]. For SAR data in the Antarctic area, atmospheric effects are limited and are therefore ignored in our study. Offset tracking is particularly applicable to the acquisition of data with long repeat intervals, and this technology allows the derivation of ice motion in areas of persistent fast-ice flow [8,16]. However, the accuracy of offset tracking is several orders of magnitude lower than that of DInSAR at a resolution of several meters. Consequently, measurements by offset tracking are not of sufficient accuracy for analysis of variation in surface velocity of the AIS (slow-ice flow). While there have been many previous studies [16–20] on changes in the surface velocity of the AIS, the spatiotemporal variation in the surface velocity of the AIS remains poorly understood. In addition, there remains little understanding of the physical mechanisms during variations in the surface velocity of the AIS and possible oceanic forcing. To better understand the dynamic processes of the AIS and the effects of its disintegration on its stability, it is essential to measure the surface velocity with high spatiotemporal resolution. This approach allows for a more comprehensive exploration of the factors influencing the ice shelf's changes.

In recent years, many scholars have used various methods to monitor the AIS's surface velocity [20–22]. They confirmed that the surface velocity showed seasonal and inter-annual variations. However, their studies did not cover the entire AIS but focused on the grounding line area or a specific glacier, due to the lack of high-spatiotemporal-resolution surface velocity extraction of the AIS and its surrounding area. A major calving event of the AIS occurred in September 2019, resulting in a loss of approximately 1.1% of its total mass [23]. The ice cavity below the Amery Ice Shelf has a complex interaction with the modified circumpolar deep water (mCDW), resulting in the freezing of the western bottom and melting of the eastern bottom of the ice shelf [24]. The physical mechanism behind the surface velocity variations in the AIS and its surrounding area, and its oceanic forcing, remain unclear. By monitoring the surface velocity of the AIS and its surrounding areas and analyzing the physical mechanisms and oceanic factors behind their spatiotemporal variations in surface velocity, we can more accurately assess the mass loss of the Antarctic Ice Sheet.

In this paper, we present a remote-sensing investigation of the spatiotemporal variations in surface velocity of the AIS for the period 2000–2022. Firstly, offset tracking was used to extract the surface velocity of the ice shelf region with fast-ice flow. DInSAR was applied to extract the surface velocity of the ice sheet with slow-ice flow, and the split-spectrum method was implemented to eliminate the ionospheric phase of InSAR pairs with serious ionospheric distraction. Then, DInSAR-based range surface velocity and offset-tracking azimuth surface velocity were combined to provide the monthly average surface velocity of the AIS. At the same time, we collected inter-annual average surface velocity products released by the Inter-mission Time Series of Land Ice Velocity and Elevation (ITS_LIVE) [25]. Finally, we investigated variations in the thickness of the AIS and the roles of possible ocean-forcing factors, including ocean temperature and fast-ice to analyze their impact on ice velocity changes. The results of this study can serve as a reference for future studies on the movement of glaciers and ice sheets in Antarctica under the effects of global climate change.

2. Materials and Methods

2.1. Inter-Annual Surface Velocity between 2000 and 2022

The present study investigated the inter-annual variation in the surface velocity of the AIS by analyzing ITS_LIVE surface velocity products. These products provide global coverage of inter-annual variation in surface velocity at a spatial resolution of 240 m from 1985 to 2022. As described in Lei, Gardner et al. [6,25], the core processing algorithm of the ITS_LIVE project utilizes a combination of a precise geocoding module "Geogrid" and an efficient offset-tracking module "autoRIFT" (autonomous Repeat Image Feature Tracking). The present study selected the surface velocity of the AIS basin from 2000 to 2022 from ITS_LIVE surface velocity products.

2.2. Intra-Annual Surface Velocity between 2017 and 2022

The present study combined the range of surface velocity derived from DInSAR with azimuth surface velocity derived from offset tracking to improve the accuracy of the surface velocity field, thereby fully utilizing the advantages of these two technologies. This approach has been widely applied to obtaining the surface velocity of polar ice sheets or glaciers [19,26]. The intra-annual surface velocity of the AIS used in this work was measured by combing multi-track Sentinel-1 single-look complex synthetic aperture radar (SAR) images acquired in the IW (interferometric wide) swath mode. This Sentinel-1 IW mode is operated as TOPS (Terrain Observation with Progressive Scan in azimuth) mode to acquire data with large swath widths (250 km) with a 3.7 m ground range and 15.6 m azimuth resolution with a repeat cycle 6 days between A and B satellites [10]. The large spatial coverage and high spatial resolution of Sentinel-1 images allow for the measurement of the monthly surface velocity of the AIS. Figure 1 shows the extent of Sentinel-1A data with five tracks.

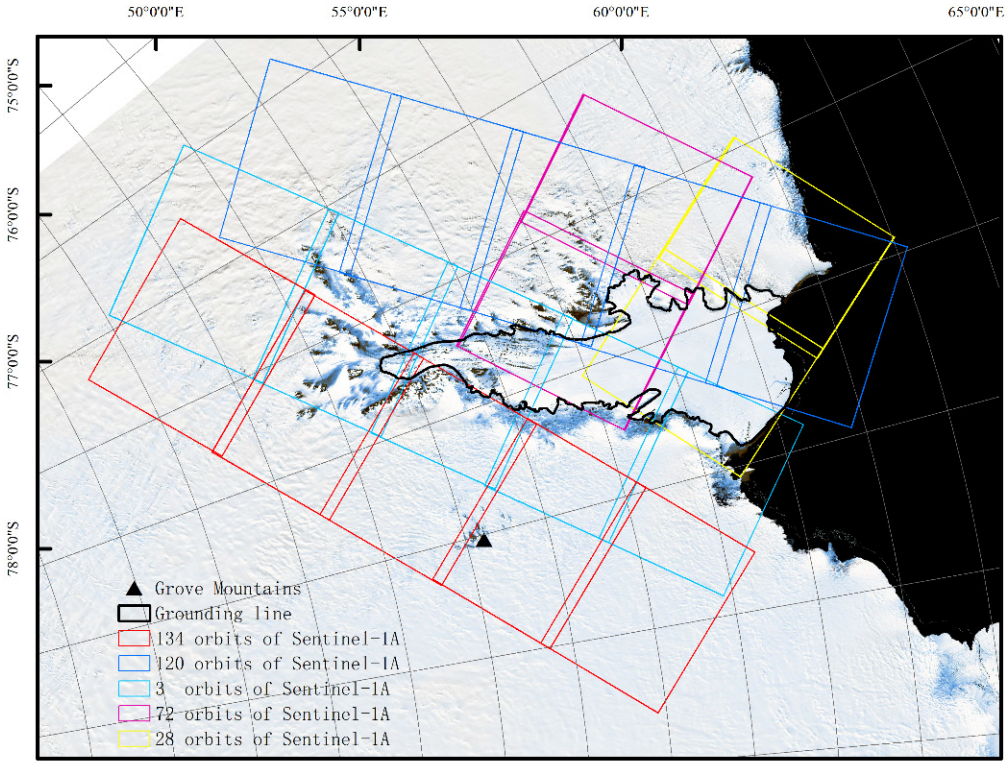

Figure 1. Map of the Amery Ice Shelf system. The different-colored polygons represent the image extent of Sentinel-1 data with different orbits used in this study.

2.2.1. The Surface Velocity Derived from Offset Tracking

The present study conducted offset tracking of interferometric synthetic aperture radar in the Scientific Computing Environment (ISCE) remote-sensing software using Sentinel-1 images to retrieve the surface velocity from 2017 to 2021. First, rough co-registration was performed between selected pairs of images. This step started with co-registration using an external digital elevation model (DEM; Reference Elevation Mode of Antarctica, RAMP) with a resolution of 100 m. Furthermore, matching techniques and spectral-diversity methods were used to refine the co-registration. The final co-registration was used to calculate the two-dimensional offsets with a search window size and step size of 640 × 128 and 40 × 10 pixels, respectively. The accuracy of the surface velocity was evaluated using abundant rock points near the AIS basin. The results had surface velocity error within 3.82 m/yr, consistent with previous related studies [1,19,20]. The accuracy in evaluated surface velocity was sufficient for analysis of variations in surface velocity in the AIS region with fast flow. Unfortunately, there were no available surface velocities for the west side of the AIS for some months each year, possibly due to surface melting or wind-blown snow.

2.2.2. The Surface Velocity Derived from DInSAR

The error in surface velocity derived from offset tracking for the AIS ice sheet region with slow-ice flow, particularly in the region in which the surface velocity is <100 m/yr, may exceed the variation in surface velocity, resulting in misinterpretation during the analysis of variation in surface velocity. Therefore, the present study combined DInSAR with Sentinel-1A images to extract the monthly average surface velocity of the AIS ice sheet regions from 2017 to 2021. The steps of DInSAR with co-registration were consistent with those of offset tracking. The interferometric phase consists of the topography, flat-earth phase, ice movement, and ionospheric phase. The interferogram has to be flattened, and the topographic phase has to be removed using a high-accuracy DEM. At the same time, the adaptive filter and multi-look processing were used to reduce the noise. To obtain ice movement in the range direction, the interferometric phase has to be unwrapped with the minimum-cost network flow (MCF) method [9]. However, frequent ionospheric disturbances in the polar region resulted in considerable contamination of the interferometric phase [27,28]. Even for Sentinel-1 SAR (C-band) images [29], the ionospheric disturbance cannot be ignored under natural phenomena such as auroras or strong magnetic storms [30]. We employed a split-spectrum method [29,31] to correct the interferometric phase with severe ionospheric disturbance in orbits 003, 134, and 090 of Figure 1. The split-spectrum method makes use of the dispersive nature of the ionospheric phase $\Delta\phi_{iono}$ to estimate and correct ionospheric signatures from the SAR images. To this end, the range spectrum of a SAR signal is typically divided into non-overlapped sub-bands with equal bandwidth. This correction process is implemented by using a bandpass filter to the range spectrum of the full-bandwidth dataset. In this process, a bandpass filter of a third of the original range bandwidth is applied, resulting in lower and upper frequency signals with slightly different center frequencies. Sub-band interferograms can then be formed within the corresponding lower and upper frequency signals. We used sub-band interferograms to estimate the ionospheric phase by

$$\phi_{low} = \Delta\phi_{iono}\frac{f_0}{f_{low}} + \phi_{non-disp}\frac{f_{low}}{f_0} \quad (1)$$

$$\phi_{upper} = \Delta\phi_{iono}\frac{f_0}{f_{upper}} + \phi_{non-disp}\frac{f_{upper}}{f_0} \quad (2)$$

$$\Delta\phi_{iono} = \frac{f_{low}f_{upper}}{f_0\left(f_{upper}^2 - f_{lower}^2\right)}\left(\phi_{low}f_{upper} - \phi_{upper}f_{low}\right) \quad (3)$$

where f_0 is the center frequency of the full-band data, f_{low} and f_{upper} are the center frequencies of the lower and upper sub-bands, respectively, and ϕ_{low} and ϕ_{upper} are the phases of the lower and upper sub-band interferograms, respectively.

The present study reduced the calculation load and time required for the correction of the data for ionospheric influences and avoided over-correction by identifying Sentinel-1 SAR data that were seriously affected by ionospheric disturbance using the geomagnetic index Kp, auroral current aggregation index AU&AL, and geomagnetic symmetric disturbance component SYM-H [27,32]. The results of the three indicators shown in Figure 2 indicated that the SAR major and slave image interferometric pair acquisition times from 31 January to 6 February 2017 coincided with major magnetic storms, whereas that from 19 January to 25 January 2017 coincided with a period of relatively little ionospheric disturbance. As shown in Figure 3B,F, the relative ionospheric phase of the interferometric pairs was estimated using the split-spectrum method. The present study analyzed the interferogram without ionospheric correction (Figure 3A,E) and the interferogram with ionospheric correction (Figure 3C,G) along the central profile line. As shown in Figure 3D,H, the surface velocity from the central profile line indicated severe ionospheric disturbance from 31 January to 6 February 2017. However, there was a minimal ionospheric disturbance from 19 January to 25 January 2017.

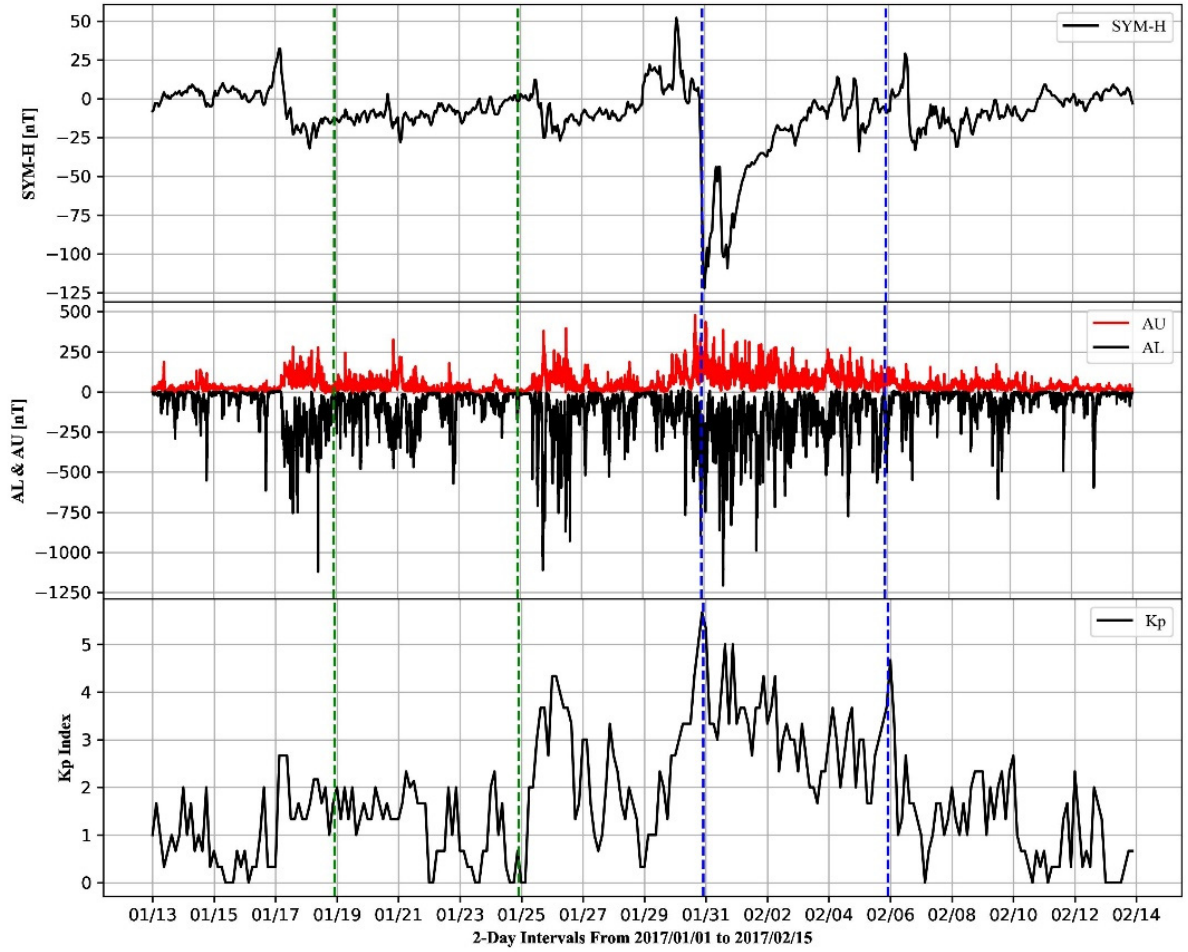

Figure 2. The variations in Kp, AU&AL, and SYM-H from 31 January to 14 February 2017. The green dashed line indicates the acquisition time of SAR image pairs from 19 January to 25 January 2017, and the blue dashed line indicates the acquisition time of SAR image pairs from 31 January to 6 February 2017. The black horizontal lines show the coordinates of the different data.

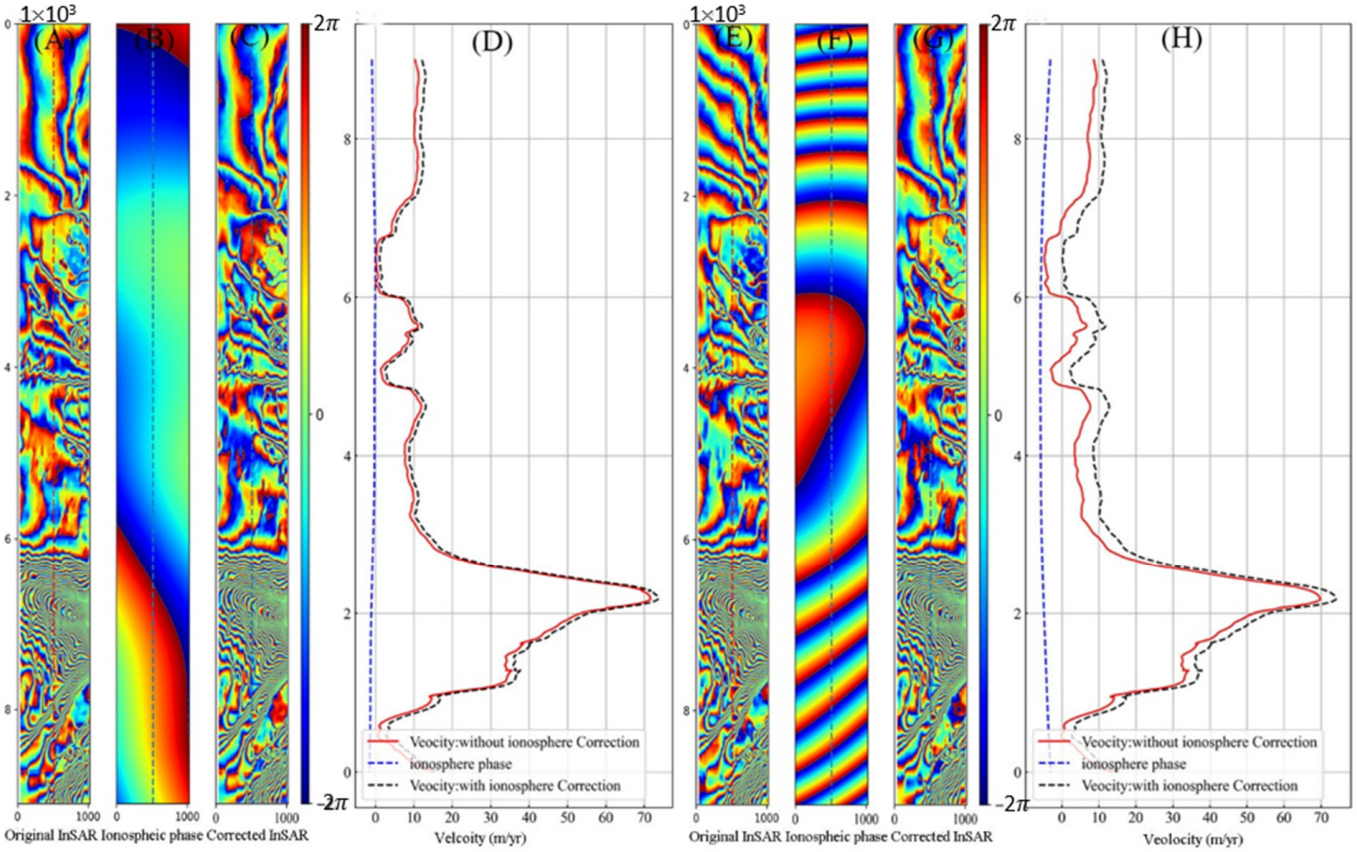

Figure 3. Comparison of interferometric phase with and without ionospheric correction. (**A**,**E**) show the interferogram without ionospheric correction. (**B**,**F**) show the relative ionospheric phase. (**C**,**G**) show the interferogram with ionospheric correction. The red dashed lines in (**A**,**E**) indicate the central profile lines and extract the interferometric phase without ionospheric correction. The blue dashed lines in (**B**,**F**) indicate the central profile lines and extract the ionospheric phase, respectively. The black dashed lines in (**D**,**H**) indicate the surface velocity with and without ionospheric correction of the central profile, respectively.

2.2.3. Combination of the DInSAR Range Surface Velocity and Offset-Tracking Azimuth Surface Velocity

For the surface velocity monitoring of large glacier–ice shelf systems in the Antarctic region, including the fast-flowing ice shelf area and the slow-flowing ice shelf surrounding area, it is difficult to extract a large glacier–ice shelf with high precision by using single DInSAR technology or offset-tracking technology. The combined method of multiple surface velocity monitoring technologies is proposed to extract the surface velocity of large ice shelves with high accuracy. The advantages of various monitoring technologies are fully utilized to extract the high-precision surface velocity results of large glacier–ice shelves. In this work, the surface velocity along the line-of-signal (slant) direction can be obtained by DInSAR. However, this contains both horizontal and vertical movement. Therefore, the incidence angle of the satellite has to be considered to estimate the ground range surface velocity v_{range}, as follows:

$$v_{range} = \frac{v_{los}}{\sin\theta} \tag{4}$$

where v_{los} is the surface velocity along the line-of-signal direction, and θ is the incidence angle of the satellite. We down-sampled the ground range surface velocity v_{range} derived from DInSAR to achieve the same spatial resolution as that azimuth surface velocity $v_{azimuth}$

derived from offset tracking. Finally, we combined the high spatial resolution and precision v_{range} and $v_{azimuth}$ [8]. The final surface velocity v is calculated by the following formula:

$$v = \sqrt[2]{v_{range}^2 + v_{azimuth}^2} \quad (5)$$

When the surface velocity results obtained from different track images were mosaicked, there were systematic deviations between adjacent tracks. Systematic deviations were removed according to the surface velocity of rock points near the AIS [19]. The surface velocity between two adjacent tracks was mosaicked by averaging the surface velocities in the overlapping area. The map of surface velocity was mosaicked from different tracks. As shown in Figure 4, this process allowed a seamless and continuous surface velocity with high accuracy to be derived.

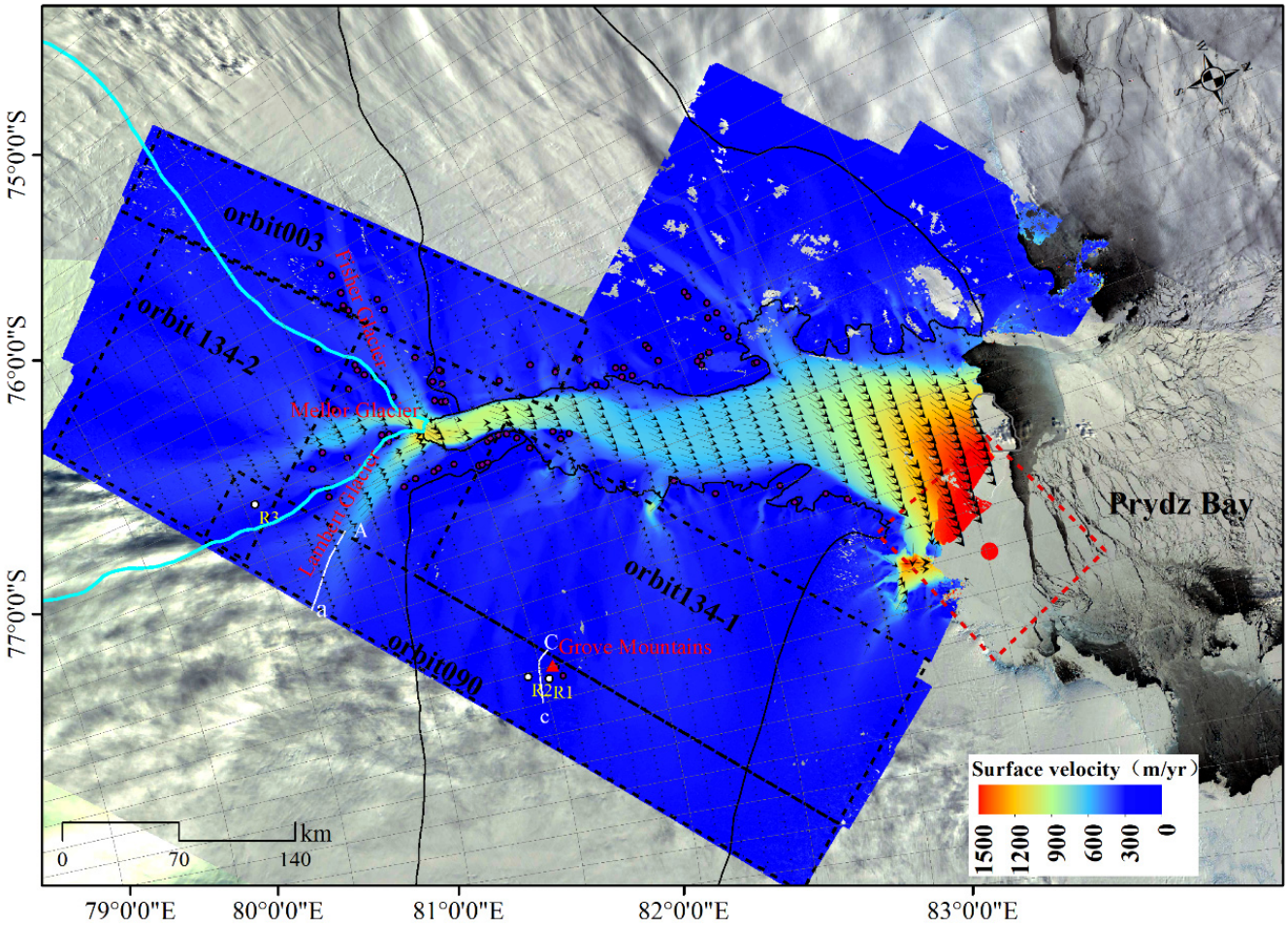

Figure 4. The seamless and continuous surface velocity of the Amery Ice Shelf (AIS) basin. The solid black line represents the boundary of the basin; the black arrow indicates the direction of flow; the bold blue FG, red MG, and black LG lines represent the ice streamlines with eight monitoring points for three different regions of the basin, respectively; the orbits 003, 134-1, 134-2, and 090 represent regions in which the data were corrected for ionospheric disturbances; the white solid line represents the profile line in orbit 090, which was used to assess the accuracy of the surface velocity corrected for disturbances by ionospheric influences in the orbit 090 region (as shown in Figure 4); the black points R1–R3 represent rock points in orbit 090 and were used to compare the surface velocity derived from offset tracking with that from DInSAR which was corrected for ionospheric factors; FG0, MG0, and LG0 of the AIS ice sheet are in orbits 003, 134-1, and 134-2 (as shown in Figure 4), respectively; the

purple points represent rock points near the AIS and were applied to assess the accuracy of ITS_LIVE surface velocity; the red dotted polygon was used to estimate the area of fast-ice attached to the AIS; D-28 represents the iceberg code; the red dot O indicates the central location in which the equivalent thickness of fast-ice according to the Estimating the Circulation and Climate of the Ocean Phase II (ECCO2) ocean model [33,34] was extracted; the solid white line in the Antarctic Ice Sheet map at the bottom left represents the AIS study area.

2.3. Ocean Temperatures

The present study investigated the effect of potential oceanic forcing on spatiotemporal variation in surface velocity of the AIS by extracting daily ocean temperatures between 2000 and 2022 from the ECCO2. The average vertical ocean temperatures between the depths of 250 m and 600 m were evaluated, corresponding to the depths of modified Circumpolar Deep Water (mCDW) linked to changes in AIS basal melt and thickness [21]. Consequently, the average ocean temperatures of ECCO2 products were extracted from three regions of the AIS front (indicated as red stars in Figure 4) between 2000 and 2022.

2.4. Fast-Ice Area and Thickness

Fast-ice appears and disappears periodically in Prydz Bay every year [35]. The present study extracted the fast-ice edge by cloud-free, true-color, moderate-resolution imaging spectroradiometer (MODIS) images with a 250 m resolution during summer. The winter fast-ice edge was manually extracted from co-registered Sentinel-1 images [36,37]. The present study obtained the total area of fast-ice (km^2) from the monthly fast-ice area for 2017 to 2022 derived from MODIS and Sentinel-1 images. A rectangular box (25 km $\times$ 25 km) representing the influence of fast-ice on the AIS front was defined (indicated by the red dotted polygon in Figure 4), and the area of fast-ice in the box was calculated. However, the area of fast-ice represents a weak index of fast-ice strength and cannot fully explain the degree of solidification of the ice body [38–40]. The thickness of fast-ice in the Antarctic winter reflects the degree of solidification of the ice body and its resistance to the AIS. As shown in Figure 4, the present study obtained the monthly equivalent thickness of fast-ice from the ECCO2 model from 2017 to 2021 based on a rectangular box centered at point O (69.625°S, 38.625°E). The variations in the area and thickness of the fast-ice area were then compared to the surface velocity of the AIS.

2.5. Thickness of the Amery Ice Shelf

The monthly average thickness of the AIS was provided by [41], which constructed a 30-year time series of monthly average surface elevation at a 5 km grid resolution for the Amery Ice Shelf spanning from 1991 to 2020 by employing a stepwise adjustment strategy and combining observations from four satellite altimetry missions—ERS-1, ERS-2, Envisat, and CryoSat-2. Building upon this, based on the hydrostatic equilibrium assumption, A 30-year time series of monthly average thickness was inverted at a 5 km grid resolution. The monthly average thickness was validated using airborne laser altimetry data from the IceBridge program and ice-penetrating radar observations from the Bedmap3 active group [40]. A comparison of the surface elevation time series with airborne laser altimetry data provided a root mean square error (RMSE) of 5.79 m and an R-squared (R2) of 0.97. As shown in Figure 5a, the thickness of the AIS ranged from 256 m to 3806 m. The monthly average thickness monitoring points are shown in Figure 5b.

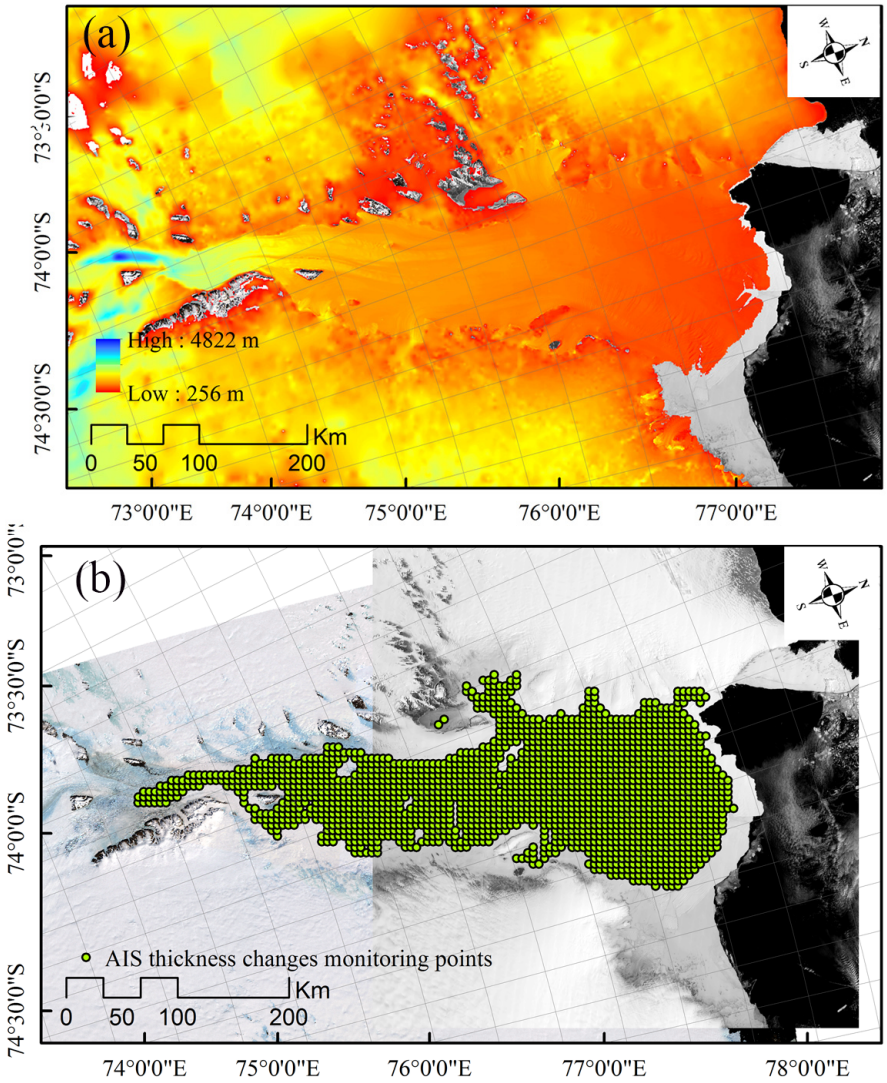

Figure 5. (**a**) AIS ice thickness; (**b**) AIS ice thickness change monitoring points. The background is a MODIS image from 21 January 2010. The solid gray line is the ground line.

3. Results

3.1. Assessment of the Accuracy of Annual Mean Surface Velocity

The present study manually selected all rock points from the georeferenced intensity image (represented by purple dots in Figure 4). The accuracy of the surface velocity provided by ITS_LIVE was evaluated by averaging the surface velocities of all rock points to produce the annual average surface velocity, as shown in Figure 6. The error in the calculated annual surface velocity ranged from 0.97 m/yr to 8.16 m/yr, with an average of 3.65 m/yr. Those errors perhaps mainly derived from the residual phase errors and the errors from the mosaicking operation. These results indicate that the errors were sufficiently small for surveying inter-annual variation in surface velocity in the AIS region from 2000 to 2022.

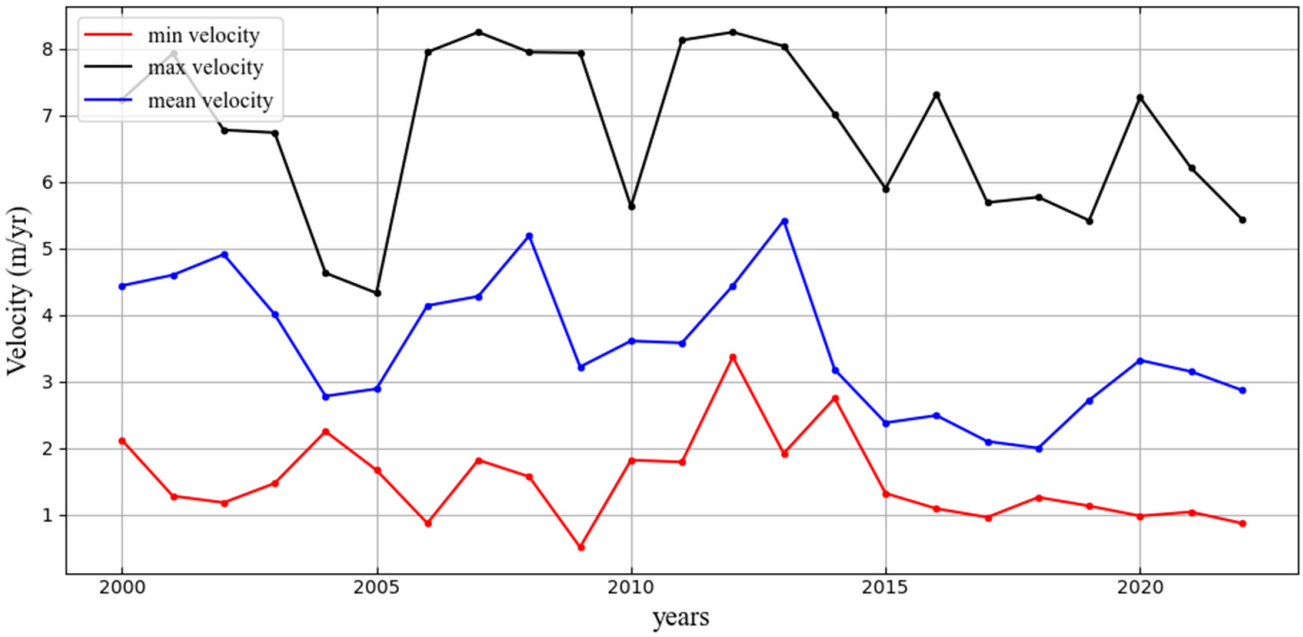

Figure 6. The accuracy of ITS_LIVE annual average surface velocity of the AIS basin from 2000 to 2022.

3.2. Assessment of the Accuracy of Monthly Average Surface Velocity

The present study combined offset tracking and DInSAR with ionospheric correction to extract monthly high-precision surface velocity in the AIS basin from 2017 to 2021. The orbits 003, 134-1, 134-2, and 090 in Figure 4 represent regions of DInSAR surface velocity with ionospheric correction calculated using the split-spectrum method. The area of orbit 090 was used as an example to investigate the performance of the surface velocity corrected for ionospheric influences. The area in orbit 090 encompasses the end of the Lambert Glacier and the Grove Mountains regions [28,31]. DInSAR-based surface velocity was compared to surface velocity from MEaSUREs [26]. A profile along the profiles Aa and Cc (white solid line in Figure 4) was extracted, and DInSAR-based surface velocity was plotted without and with ionospheric correction, as shown in Figure 7. DInSAR-based surface velocities without ionospheric correction at profiles Aa and Cc deviated significantly from surface velocities from MEaSUREs (Figure 7A,B). These deviations reach 6 m/yr in the Lambert Glacier region and 4.1 m/yr in the Grove Mountains region. DInSAR-based surface velocities with ionospheric correction at Aa and Cc were consistent with surface velocities from MEaSUREs (Figure 7C,D), suggesting the need for ionospheric correction of DInSAR-based surface velocities for the AIS ice sheet region.

The present study further evaluated the errors in surface velocities obtained by three methods: (1) only offset tracking, (2) combining offset tracking and DInSAR without ionospheric correction, and (3) combining offset tracking and DInSAR with ionospheric correction. The errors in the surface velocities of rock points R1–R3 in orbit 090 (Figure 4) were then evaluated using the above three methods, as shown in Table 1. The results showed that the maximum error of method (1) surface velocities at the three rock points was 3.82 m/yr, whereas that of method (2) surface velocities was 1.77 m/yr, similar to MEaSUREs-based surface velocity. The maximum error of method (3) was 0.28 m/yr, which was sufficiently small to allow for the analysis of variations in the monthly average surface velocity of the AIS ice sheet.

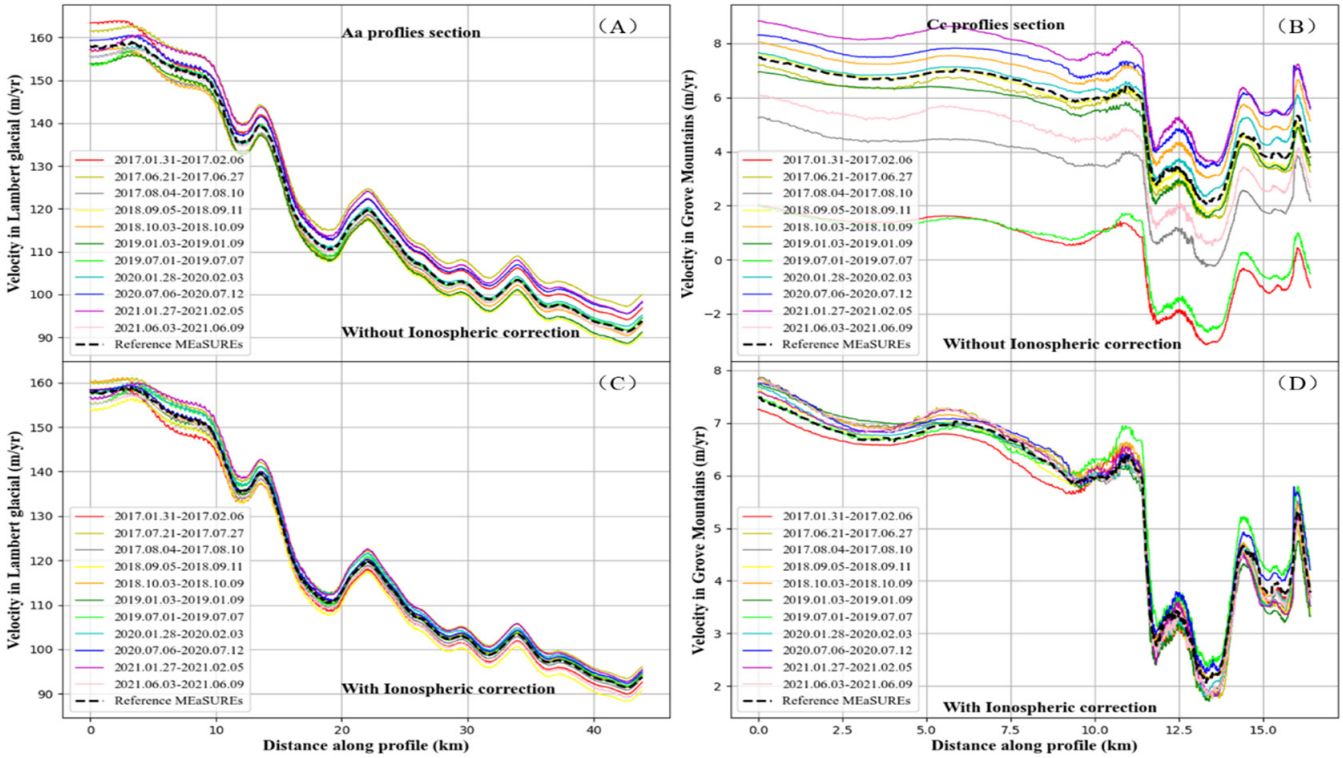

Figure 7. The orbit 090 time-series surface velocity profile analysis without and with ionospheric correction. (**A**,**B**) represent reference surface velocity from MEaSUREs (gray dotted line) and DInSAR-derived surface velocity without ionospheric correction (other-colored lines) from profiles Aa and Cc, respectively. (**C**,**D**) represent reference surface velocity from MEaSUREs (gray dotted line) and DInSAR-derived surface velocity with ionospheric correction (other-colored lines) from profiles Aa and Cc, respectively.

Table 1. Comparison of three methods at rock points R1–R3 from 2017 to 2021.

Points	R1 (m/yr)				R2 (m/yr)				R3 (m/yr)			
Methods	**(1)**	**(2)**	**(3)**	**MEaSUREs**	**(1)**	**(2)**	**(3)**	**MEaSUREs**	**(1)**	**(2)**	**(3)**	**MEaSUREs**
Mean	1.77	0.25	2.8	1.74	1.84	0.20	3.2	1.16	1.68	0.28	3.82	1.43
Standard	1.81	0.28	1.28	0.23	1.73	0.21	2.03	0.16	1.75	0.15	2.56	0.17

As shown in Figure 8, the present study also compared the variations in DInSAR-based surface velocity with and without ionospheric correction at three monitoring points (FG0, MG0, and LG0) in the AIS ice sheet region (Figure 2) from 2017 to 2021. The results indicated that surface velocity with ionospheric correction at LG0 showed significant seasonal variation from 2017 to 2021. However, there were no significant seasonal changes in surface velocity with ionosphere correction at FG0 and MG0.

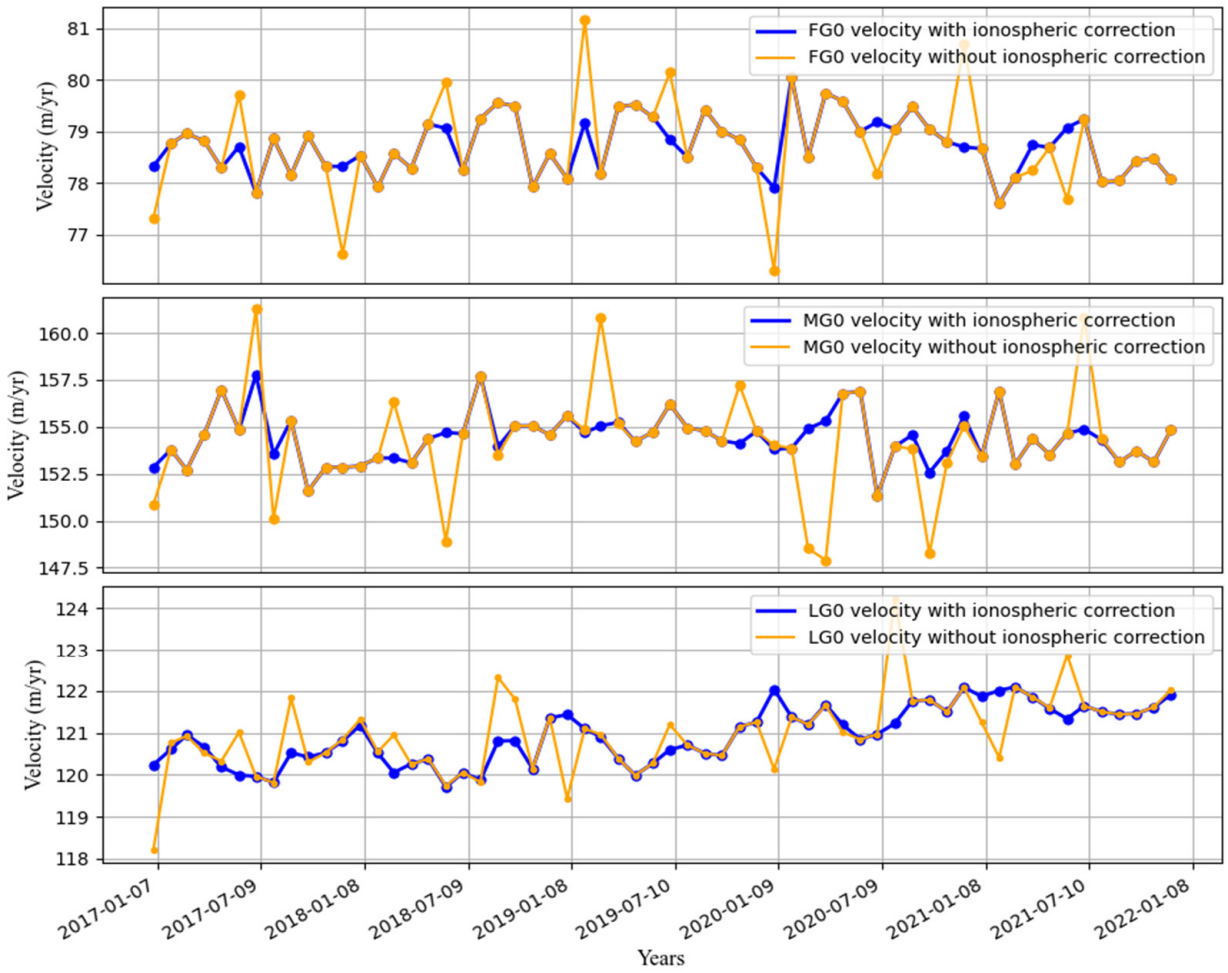

Figure 8. Comparison of surface velocities of DInSAR-based with and without ionospheric correction at FG0, MG0, and LG0 from 2017 to 2021.

3.3. Inter-Annual Variation in Surface Velocity from 2000 to 2022

As shown in Figure 9, the present study extracted ITS_LIVE inter-annual surface velocity at eight monitoring points on three ice streamlines (FG, MG, and LG) from 2000 to 2022. As shown in Figure 10, the variations in the inter-annual surface velocity at all monitoring points indicated an acceleration in the surface velocity of the LG ice streamline (eastern AIS). There was a deceleration in the surface velocity of the MG ice streamline (central ice streamline), except that at MG7, which accelerated. Similarly, there was a deceleration in the surface velocity of the FG ice streamline (western AIS), except that at FG7, which was stable.

A comparison of the variations in surface velocity at LG7, MG7, and FG7 in the AIS front showed acceleration in the surface velocity of the AIS front, with the highest acceleration at LG7 (eastern AIS), in which surface velocity increased by 14.7% (average annual acceleration of 20.5 m/yr), followed by MG7 (central AIS front), in which surface velocity increased by 9.2% (annual an acceleration of 9.5 m/yr). The surface velocity at FG7 (western AIS) was relatively stable.

A comparison of changes in surface velocity at LG2, MG2, and FG2 near the southernmost grounding line of the AIS showed an acceleration in the surface velocity of LG2 (eastern side of the grounding line), increasing by 2.57% (average annual acceleration of 0.6 m/yr). The remaining monitoring points (LG3–LG6) on the LG ice flow line showed similar accelerations in surface velocity to that of LG2. However, the surface velocity of MG2 (central region of the southernmost grounding line) and FG2 (western side of the southernmost grounding line) decreased by 4.3% (average annual deceleration of 0.77 m/yr)

and 3.9% (annual a deceleration of 0.58 m/yr), respectively. Other monitoring points of the MG ice streamlines (MG3–MG6) and FG ice streamlines (FG3–FG6) showed similar decelerations in surface velocity to that of MG2 and FG2.

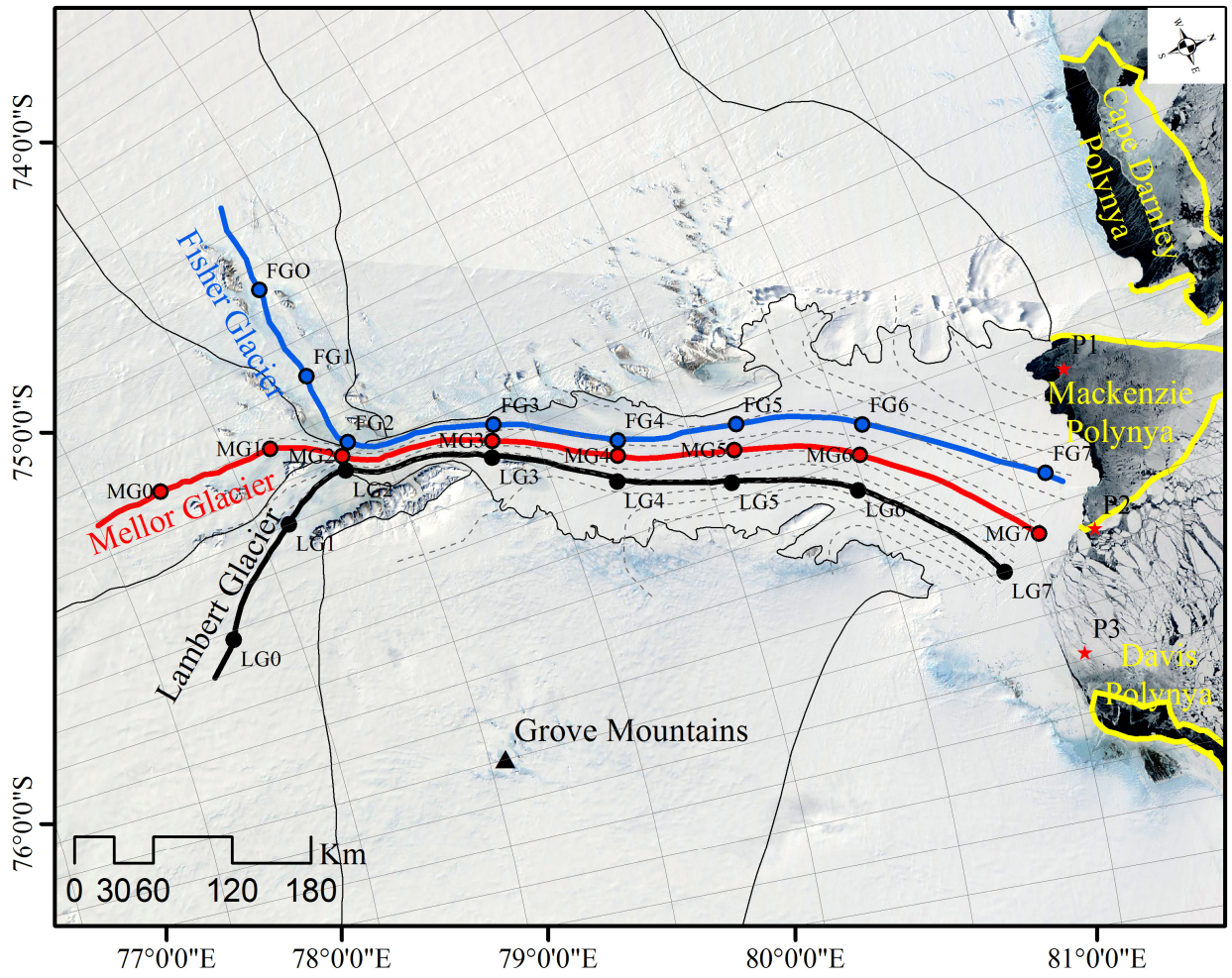

Figure 9. Ice streamlines of the Amery Ice Shelf (AIS). The gray dotted lines represent ice streamlines; the blue, red, and black lines represent the FG, MG, and LG ice streamlines in three main regions on the western, middle, and eastern sides of the AIS, respectively, with eight monitoring points located at each ice streamline; the gray line represents the grounding line; the blue arrow indicates the direction of the mCDW in the ice cavity; the yellow lines represent the boundaries of the polynyas in August 2018; the red arrows represent the clockwise cyclonic gyre (Prydz Gyre). The present study estimated the average ocean temperatures at a depth of between 250 m and 600 m from positions represented by the red stars (P1–P3).

Both LG0 and LG1 of the LG ice streamlines are in the AIS ice sheet region, and both showed relatively small changes in surface velocities. LG1, 60 km from the southernmost grounding line, showed a slight increase in surface velocity of 0.15% (an average acceleration of 0.24 m/yr), whereas LG0, 120 km from the southernmost grounding line, showed a stable surface velocity. MG0 and MG1 of the MG ice streamline and FG0 and FG1 of the FG ice streamlines also lie in the AIS ice sheet region. The surface velocities of MG1 and FG1, both 60 km from the southernmost grounding line, decreased slightly by 0.11% (average annual deceleration of 0.20 m/yr) and 0.3% (an average deceleration of 0.18 m/yr), respectively. MG0 and FG0, 120 km from the southernmost grounding line, showed stable surface velocities.

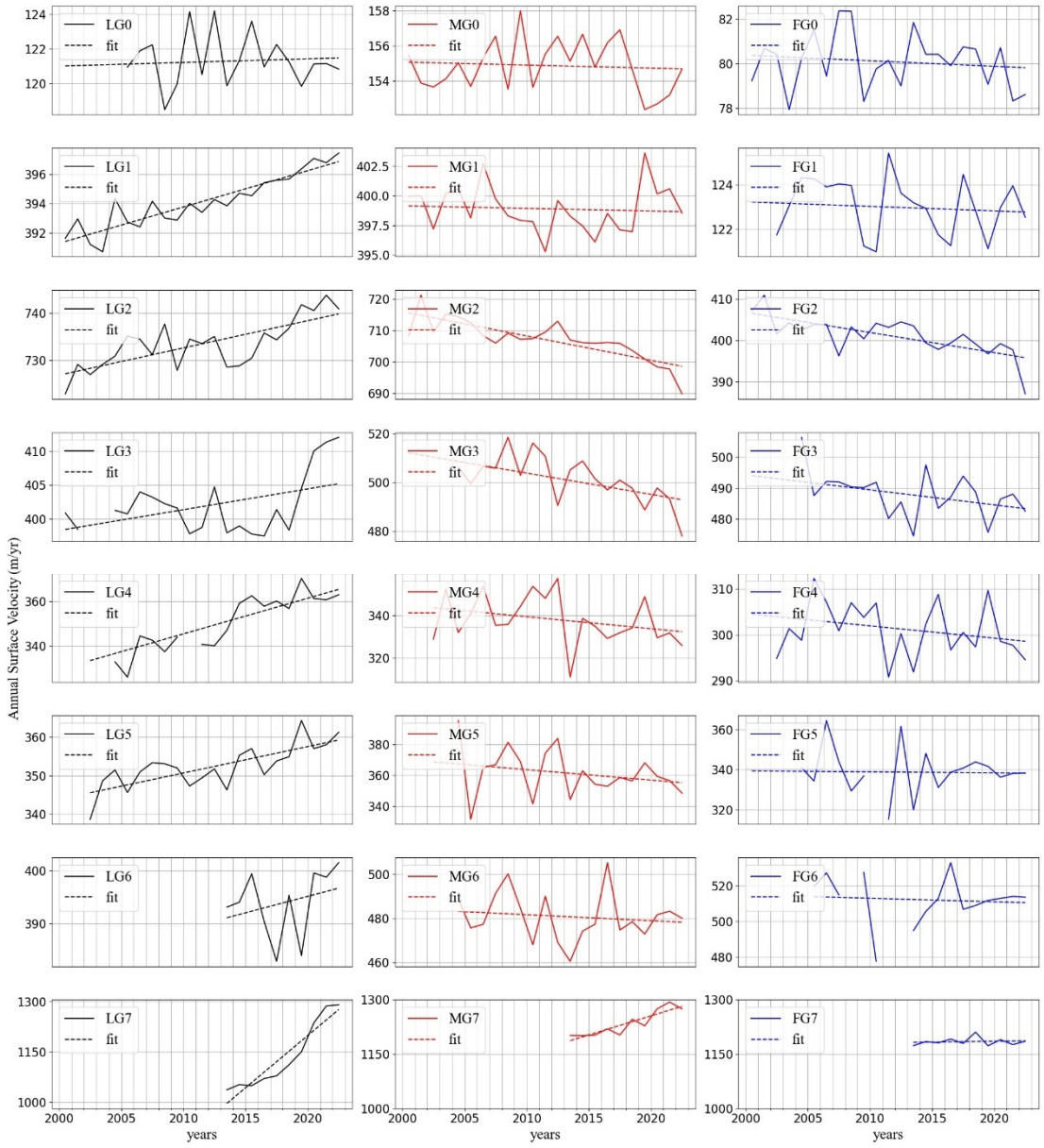

Figure 10. Inter-annual surface velocity changes at eight monitoring points of the FG, MG, and LG ice streamlines from 2000 to 2022.

3.4. Seasonal Variation in Surface Velocity from 2017 to 2021

As shown in Figure 9, the present study extracted the intra-annual variation in surface velocity at all monitoring points of the FG, MG, and LG ice streamlines from 2017 to 2021. As shown in Figure 11, the variation in the monthly average surface velocity in the three regions of the AIS was analyzed. From the surface flow velocity changes of the MG and LG ice flow lines in Figure 11, the surface velocity changes of the two ice flow lines can be seen, but the seasonal changes are not obvious. However, the surface velocities of all monitoring points of the LG ice streamlines showed significant seasonal variations, and the highest and lowest surface velocities were in summer and winter, respectively. Among all the monitoring points of the LG ice streamline, the surface velocity at LG7, in the AIS front, decelerated from March to September at an average rate of 21.7 m/yr, then it accelerated from October to February of the following year, at an average rate of 44.3 m/yr. The acceleration in summer surface velocity exceeded the deceleration in winter surface velocity by a factor of two, resulting in an overall acceleration in annual surface velocity at LG7. Seasonal variations in surface velocities at other monitoring points on

the LG ice streamline (eastern side of the AIS) were similar to that at LG7, although the magnitudes of variations were smaller. Table 2 shows a comparison of surface velocities of all monitoring points on the LG ice streamline. The results showed that the AIS front (LG7) had the highest magnitudes of variations in surface velocity, followed by those at the southernmost grounding line (LG2), followed by those at the ice shelf (LG3–LG6), with those at the ice sheet (LG0–LG1) being the smallest. This result can be attributed to the sensitivity of the AIS front to changes in the marine environment due to its direct contact with the ocean. In contrast, since the ice sheet is away from the sea, variation in its surface velocity is less sensitive to changes in the marine environment.

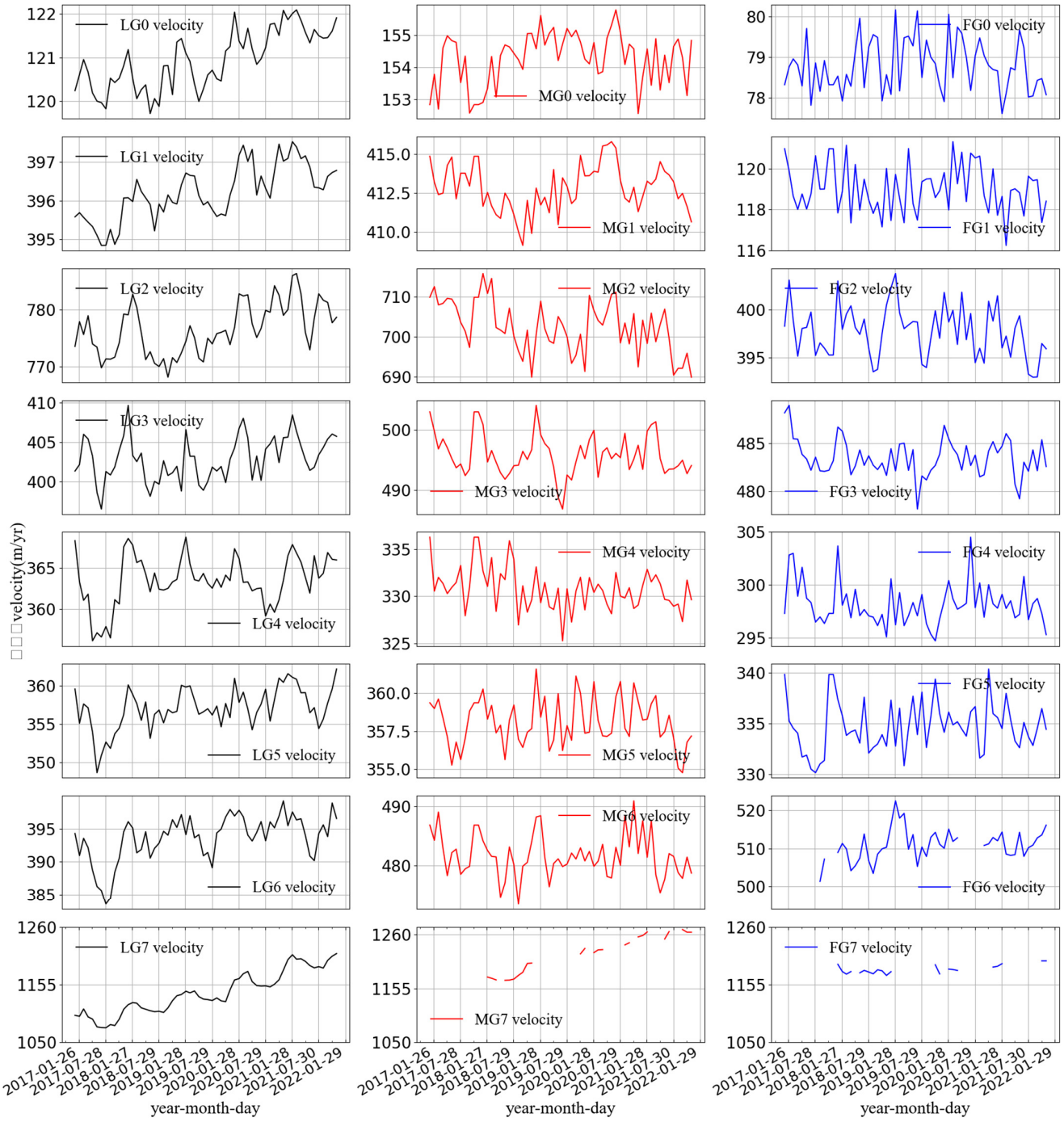

Figure 11. Intra-annual surface velocity variations at eight monitoring points of the LG, MG, and FG ice streamlines from 2017 to 2021.

Table 2. Comparison of the parameters of surface velocity among eight monitoring points on the LG ice streamline.

Monitoring Point	Maximum (m/yr)	Minimum (m/yr)	Magnitude (m/yr)
LG0	122.1	119.7	2.4
LG1	397.5	394.8	2.7
LG2	786.3	768.2	18.1
LG3	398.2	409.64	11.5
LG4	368.8	363.5	12.7
LG5	362.1	350.1	12.0
LG6	399.2	387.3	11.9
LG7	1246.6	1076.1	170.5

The absence of monthly average surface velocities for FG7 and MG7 for some months prevented an accurate assessment of the variations in surface velocity. However, the present study determined that surface velocity at MG7 was accelerating, whereas that at FG7 was relatively stable. A comparison of surface velocities at FG7, MG7, and LG7 showed that their rank according to the acceleration in surface velocity was LG7 > MG7 > FG7.

4. Discussion

Previous studies have shown spatially uneven and temporally periodic variations in the surface velocities of ice shelves and glaciers [42]. Variations in surface velocities can be attributed to a variety of physical mechanisms, mainly including (1) a change in the viscosity of the ice body leading to variations in ice flow [43], (2) changes in the buttressing force of the ice shelf resulting from the disappearance or growth of impediments (such as fast-ice and ice shelf calving) in the ice shelf front [44,45], and (3) basal melting and refreezing of the ice shelf, resulting in thinning and thickening of the ice shelf [4,5,46]. The present study surveyed variations in the surface velocity of the AIS in response to possible ocean forcing and analyzed the physical mechanisms responsible.

4.1. Analysis of Factors of Inter-Annual Variation in Surface Velocity

By considering the thickness of the AIS front and the mCDW depth, the present study calculated the average ocean temperature at depths of 250 m to 600 m in three regions (P1–P3, indicated by red, five-pointed stars in Figure 9) near the coastline of the AIS front [22]. Figure 12 shows the ECCO2-derived daily ocean temperatures of the AIS front from 2000 to 2022. The results showed inconsistent changes in the magnitudes and peaks in ocean temperature in P1–P3 (Figure 9). The ocean temperature of P2 between 2000 and 2007 slightly exceeded those of both P1 and P3 by 0.10 °C, whereas that of P3 between 2008 and 2022 exceeded those of P2 and P1 by 0.25 °C and 0.85 °C, respectively.

Several oceanic models [24,47,48] have confirmed a clockwise circulation in the AIS ice cavity from east to west (the blue arrow on the AIS in Figure 9) via the Prydz Gyre. This circulation can be attributed to the inflow of the warm mCDW into the eastern side of the AIS and the outflow of the cold mCDW from the western side of the AIS. Previous studies have observed the path of mCDW intrusions in May 2012 using MEOP-CDT data [49,50]. The strong eastward jet along the eastern branch of the cyclonic Prydz Bay gyre at a depth of between 250 m and 400 m represents the main pathway for mCDW (red arrows in Figure 9) flow toward the eastern side of the AIS front [48]. A portion of the mCDW flows southward along the eastern side of the AIS and circulates clockwise from east to west near the southernmost grounding line of the AIS. The warm mCDW mixes with the meltwater in the cavity, thereby reducing the temperature of the mCDW in the western AIS. Another part of the mCDW circulates clockwise from east to west in the central region of the AIS. This circulation mixes with meltwater, thereby also causing a reduction in the ocean temperature of the mCDW [47,50]. Following a mix of the two parts of the mCDW, meltwater flows out from the western side of the AIS front, eventually moving toward the McKenzie polynya.

During the circulation of mCDW in the AIS ice cavity [43,47], the warm mCDW contributes to the basal melting of the eastern AIS (melting rate of 1.8 ± 0.3 m/yr), thereby decreasing the thickness of the AIS. At the same time, the cold mCDW contributes to basal refreezing of the central and western regions of the AIS (refreezing rate of 1.8 ± 0.3 m/yr), resulting in a thicker AIS.

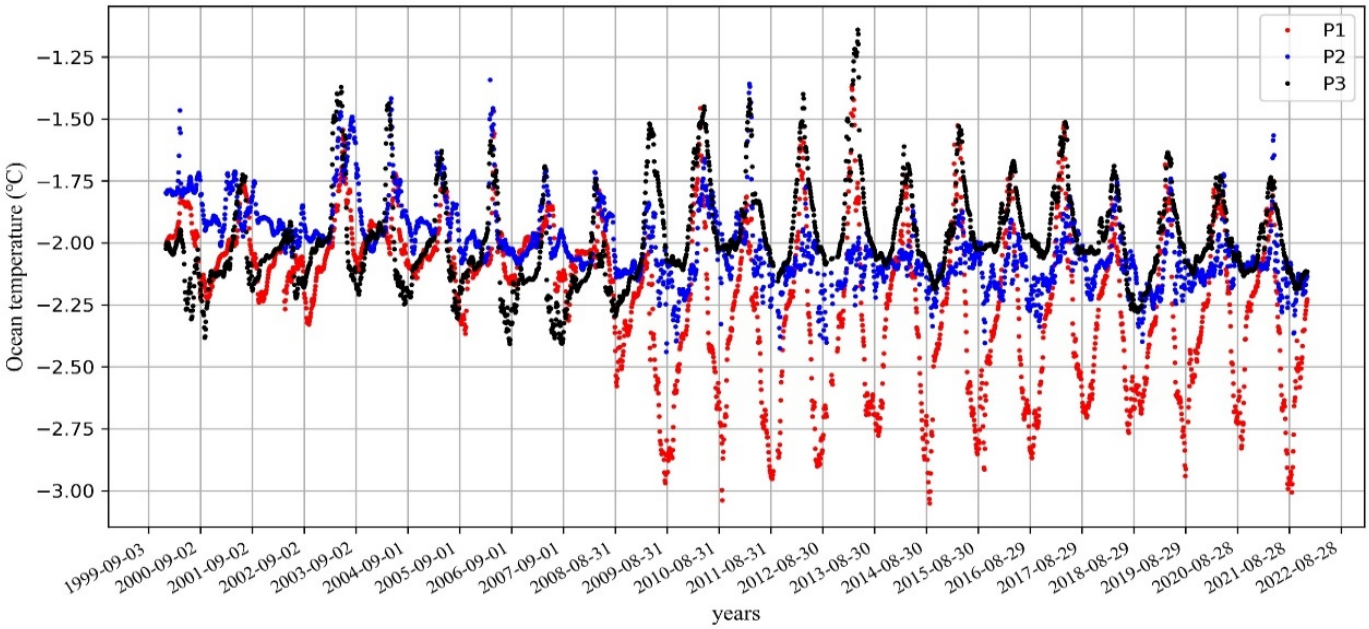

Figure 12. The ECCO2 time-series daily ocean temperatures of the AIS front region from 2000 to 2022.

As shown in Figure 13, the present study compared the variations in the surface velocities of all monitoring points of the FG, MG, and LG ice streamlines with variations in the thickness of the AIS. Unfortunately, only the variations in the thickness of the ice shelf were obtained. However, no data were obtained for the ice sheet (Figure 5). The results indicated an acceleration in the surface velocity of the LG ice streamline between 2000 and 2022, resulting in a decrease in ice thickness. Besides the acceleration in surface velocity and decrease in ice thickness of MG7, surface velocities at MG2–MG6 decreased, whereas there were increases in ice thickness. Except for FG7, in which surface velocity and ice thickness remained stable, the surface velocities at FG2–FG6 decreased, whereas their ice thicknesses increased. The ocean temperature of P1 exceeded that of P2, which in turn exceeded that of P3. The corresponding acceleration in the surface velocity of LG7 exceeded that of MG7, whereas the surface velocity at FG7 was relatively stable. These results suggested that the ocean temperature at the AIS front was the main factor driving variations in surface velocity at FG7, MG7, and LG7 in the AIS front.

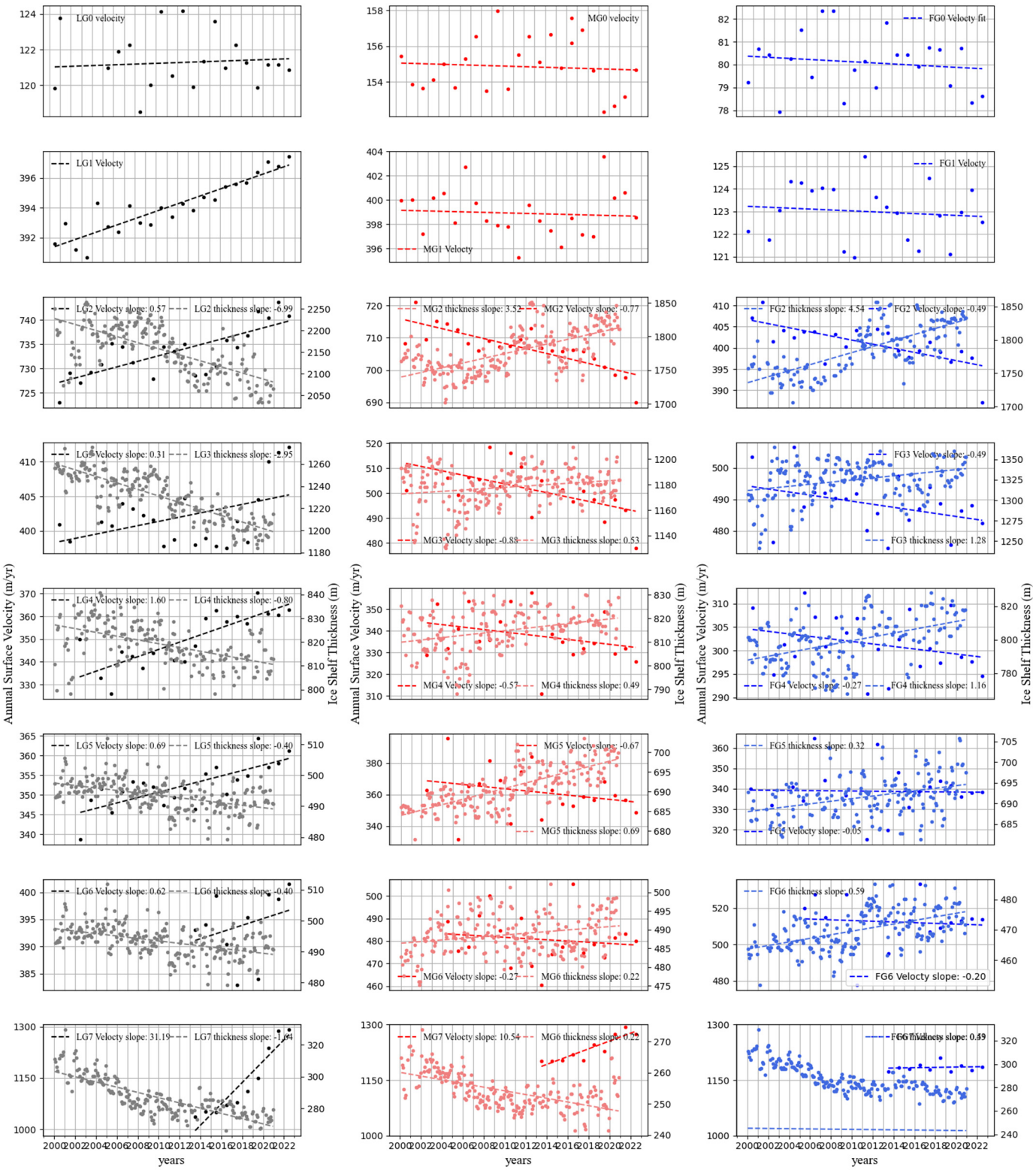

Figure 13. Compare the inter-annual surface velocity and ice thickness change at all monitoring points of FG, MG, and LG ice streamlines from 2000 to 2022.

4.2. Effect of Fast-Ice on Variations in Intra-Annual Surface Velocity

The present study estimated the area of fast-ice attached to the AIS front and calculated its equivalent thickness using the ECCO2 model [34] between 2017 and 2022. Figure 14 shows the changes in the area of fast-ice in the AIS front between summer and winter. To compare fast-ice area changes, we get a maximum and minimum fast-ice extent for each year and the total area in square kilometers for pair of images in the red boxes. The results showed seasonal growth and retreat in fast-ice on the eastern side of the AIS front. In contrast, there was no fast-ice in the western and middle regions of the AIS front, in which the Mackenzie polynya persists (Figures 9 and 14). These results suggest that fast-ice does not affect the surface velocities of the western and middle regions (FG and MG ice streamlines), thereby possibly explaining the lack of seasonal variation in the surface velocities of the western and central regions. Therefore, the present study only extracted the area and thickness of fast-ice for the eastern region of the AIS front (88.875°S, 75.875°E) representing the central grid unit (point O in the red dotted box in Figure 14). The influences of variations in the area and thickness of fast-ice on the surface velocity of the LG ice streamline were then assessed. LG7 on the LG ice streamline is closest to the fast-ice region and most sensitive to changes in fast-ice. As shown in Figure 15, the present study analyzed the relationship between variations in the area and thickness of fast-ice at LG7 and surface velocity. The results showed increases in the area and thickness of fast-ice from February to July, an increase in the buttressing force of fast-ice, and a decrease in the surface velocity of LG7 at a rate of 20.1 m/yr. There was a slight decrease in the area of fast-ice from July to September, whereas its thickness continued to increase, increasing its buttressing force. This resulted in a slight decrement in surface velocity at a rate of 1.5 m/yr. These results suggested that the thickness of fast-ice had a slightly bigger effect on its buttressing force than its area. The area and thickness of fast-ice rapidly decreased from October to February of the following year. This resulted in a sharp decrease in its buttressing force and an acceleration in surface velocity at LG7 at a rate of 44.3 m/yr. The acceleration in surface velocity at LG7 exceeded deceleration by a factor of two, resulting in an overall acceleration in the annual average surface velocity in the eastern region of the AIS. In addition, the magnitudes of variations in surface velocities at the other monitoring points of the LG ice streamline were relatively small. This result can be attributed to LG being relatively far from the fast-ice region and therefore less sensitive to variations in fast-ice. Although there were seasonal variations in surface velocity, the magnitudes of variation were small.

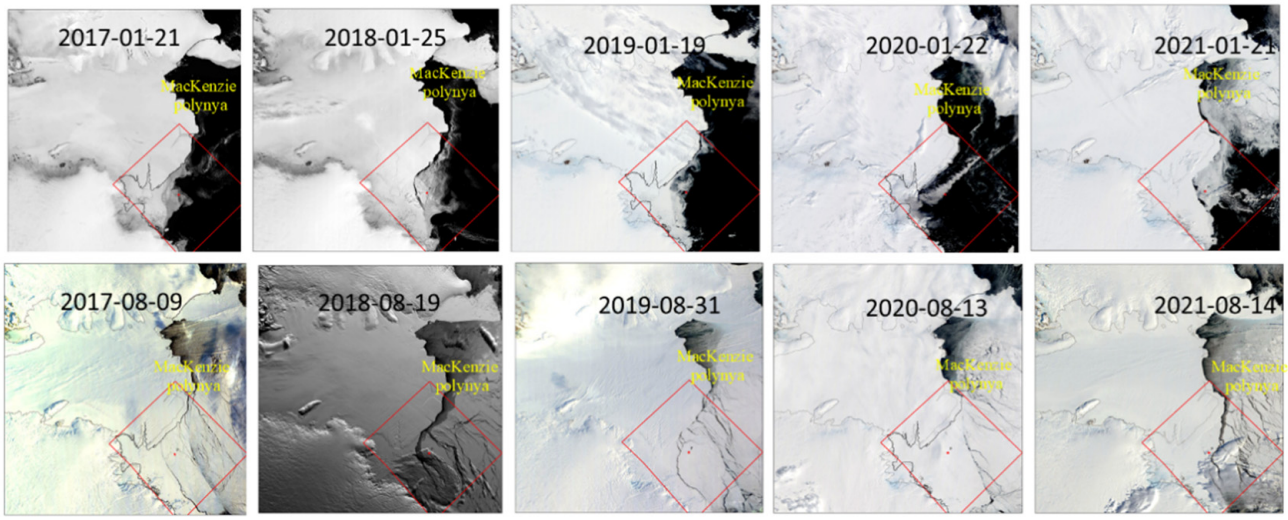

Figure 14. The fast-ice in the AIS front was extracted from the MODIS images in summer (January) and winter (August). The red box delimits the area used for detailed fast-ice analysis.

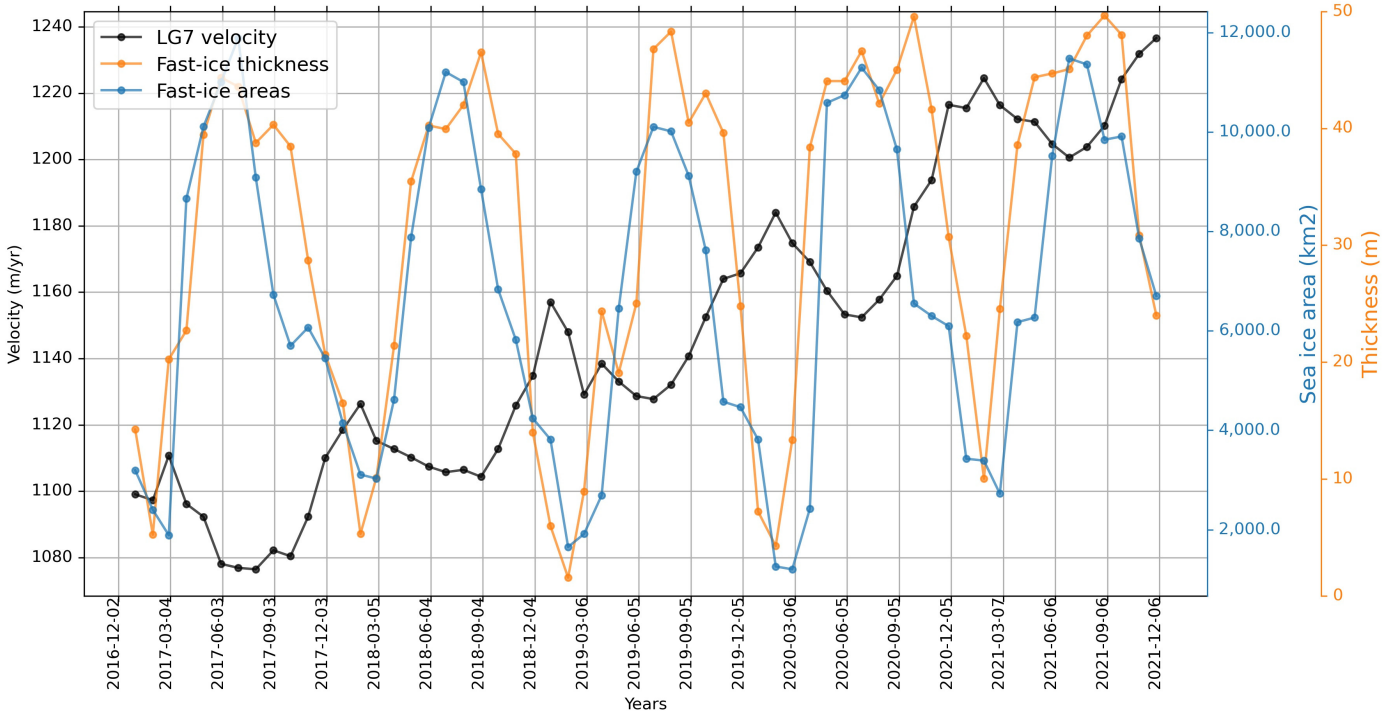

Figure 15. The AIS front fast-ice area and equivalent thickness are compared with the LG7 surface velocity from 2017 to 2021.

4.3. Effect of Ocean Temperatures on Seasonal Variations in Surface Velocity

Recent studies have demonstrated strong seasonal variation in the average ocean temperature of the AIS front [24,47,50]. There is usually an increase in ocean temperature from December to May of the following year, reaching a peak in June (>−1.8 °C), whereas the ocean temperature decreases from June to November, reaching a minimum in November (<−2.1 °C). As shown in Figure 16, the present study examined the relationships between the ocean temperature of P3 (indicated as the red star in Figure 9) and the surface velocities at all monitoring points of the LG ice streamlines from 2017 to 2021. The results showed that the variations in surface velocity at all monitoring points were positively correlated with variations in ocean temperature. These results suggested that the front region of the AIS (LG7), characterized by a surface velocity of ~1250 m/yr, is most sensitive to variation in ocean temperature, whereas the southernmost grounding line region (LG2), characterized by a surface velocity of ~750 m/yr, is relatively sensitive to variation in ocean temperature. The eastern side of the AIS (LG3–LG6), characterized by a surface velocity of between 350 m/yr and 400 m/yr, was the least sensitive to variation in ocean temperature. The results of the present study were consistent with those of other studies [20,51] and showed that the surface velocity of the ice shelf was positively correlated with variations in ocean temperatures.

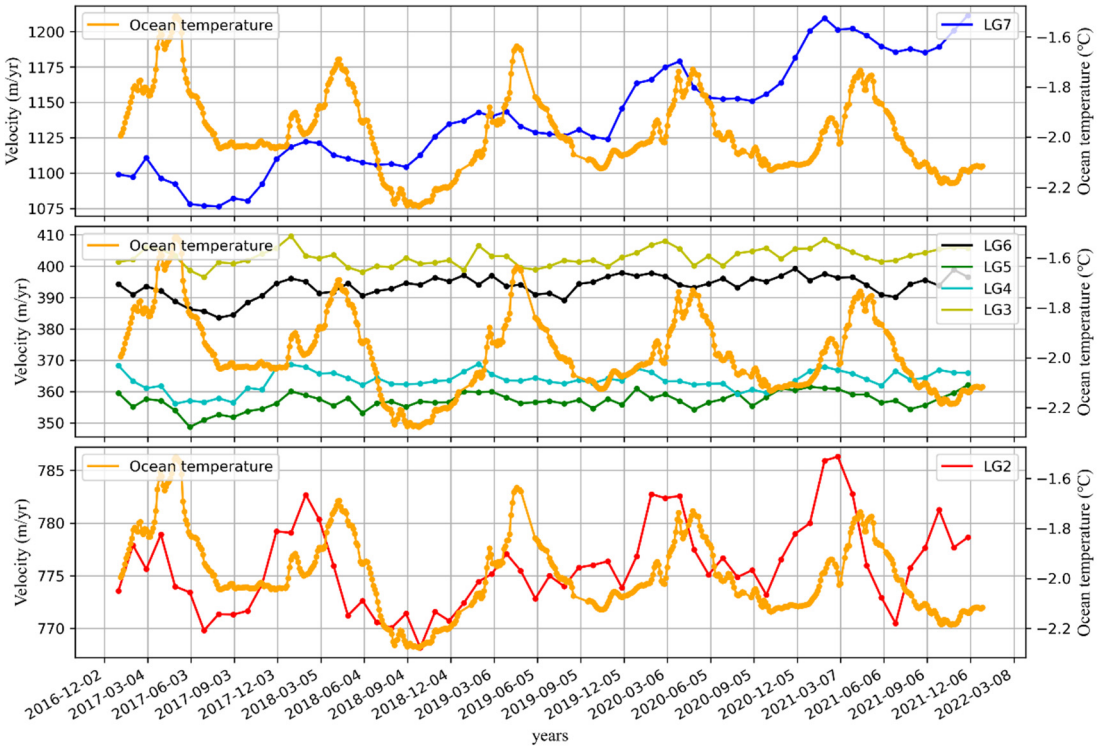

Figure 16. Comparison between the P3 ocean temperature and the surface velocity of the LG ice streamline from 2017 to 2021.

4.4. Effect of Ice Shelf Calving on Variation in Surface Velocity

Iceberg D-28 calved from the AIS front on 25 September 2019. This calving event was the largest since the early 1960s [52]. The present study analyzed the difference in surface velocity before (June 2019) and after (November 2019) the calving event. The results showed no significant difference in surface velocity before and after the event near the calved area (Figure 17a). The buttressing effect on the stress regime within the ice was then quantified to investigate the response of surface velocity to the calving event [53]. At a maximum buttressing of ≤ 0.3, the calving event did not affect the variation in surface velocity of the ice shelf [54]. As shown in Figure 17b, the maximum buttressing force of the calved area was less than 0.3. These results suggested that the area calved from the AIS was within a zone in which a calving event would not affect variation in the surface velocity of the AIS.

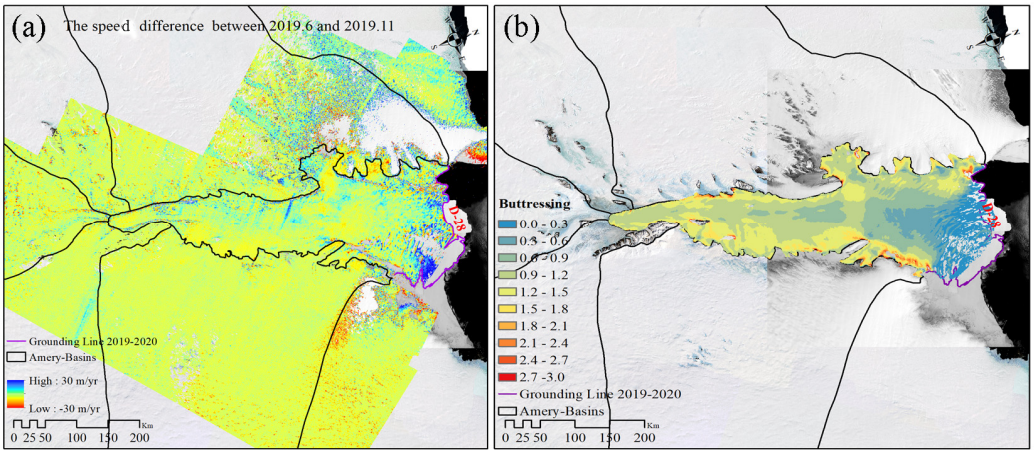

Figure 17. (**a**) represents the difference in surface velocity before (June 2019) and after (November 2019) the ice shelf calved. (**b**) Maximum buttressing of AIS derived from [55].

5. Conclusions

This study employs DInSAR and offset-tracking techniques to derive the monthly average surface velocities of the Amery Ice Shelf and its surrounding regions from Sentinel-1A imagery spanning 2017 to 2022. Combined with the inter-annual ice velocity product of ITS_LIVE from 2000 to 2022, we investigated the spatiotemporal variations in surface velocities within the AIS and its surrounding areas.

Based on the analysis of inter-annual surface velocity in AIS and its surrounding areas from 2000 to 2022, we found that the variations in surface velocity are not consistent in different spatial regions of the AIS. There was a decrease in surface velocity in the central and western regions of the AIS, whereas that in the eastern region increased. Variation in surface velocity on the AIS's surrounding areas was less than that of the Amery Ice Shelf itself, which in turn was less than that of the Amery Ice Shelf front. In addition, the ice sheet far from the southernmost grounding line of the AIS showed little variation in surface velocity from 2000 to 2022. These results could mainly be attributed to the contribution of the clockwise circulation of mCDW in the AIS ice cavity to the basal melting of the eastern AIS, resulting in a decrease in ice thickness and increased surface velocity in the eastern section. The circulation process also contributed to the basal refreezing of the central and western regions of the AIS, causing an increased ice thickness and decreased surface velocity in the central and western sections.

Based on the analysis of monthly average surface velocity changes in the Amery Ice Shelf and its surrounding areas, we found that there was no significant seasonal variation in the monthly surface velocity of the central and western regions of the AIS, which may be related to the persistent Mackenzie polynya. The surface velocity of the eastern AIS front fluctuated seasonally under the combined effect of the area and thickness of fast-ice. In addition, the seasonal variation in ocean temperature was another factor influencing the seasonal variation in surface velocity in the eastern side of the AIS. The calving event on the AIS front on 28 September 2019 had no impact on the variation in surface velocity, which could be attributed to the location of the calved area in the safety belt [54,55].

An investigation of the spatiotemporal variation in the surface velocity of the AIS and the underlying physical mechanism showed uneven inter-annual spatial variation in the surface velocity of the AIS. In addition, there was seasonal variation in the monthly average surface velocity of the eastern side of the AIS. However, the variation in the surface velocity of the AIS was of minimal magnitude, suggesting that the AIS basin has remained relatively stable over the past two decades.

Author Contributions: Conceptualization, Y.M. and Z.W.; methodology, B.Z.; software, F.L.; validation, Y.M., B.Z. and H.G.; formal analysis, Y.M.; investigation, Y.M.; resources, Z.W.; data curation, B.Z.; writing—original draft preparation, Y.M.; writing—review and editing, Y.M.; visualization, Y.M.; supervision, B.Z.; project administration, J.A.; funding acquisition, B.Z. and Z.W. All authors have read and agreed to the published version of the manuscript.

Funding: This work was supported by the National Natural Science Foundation of China (grant nos. 41941010), Hubei Provincial Natural Science Foundation of China (grant nos. 2023AFB591), and the Fundamental Research Funds for the Central Universities (grant nos. 2042024kf0016, 2042022dx0001). The authors declare no conflict of interest.

Data Availability Statement: The MODIS and SAR images were accessed via the websites https://www.earthdata.nasa.gov/worldview (accessed on 9 May 2024) and https://www.polarview.aq/antarctic (accessed on 9 May 2024), respectively. The ECCO2 time-series ocean temperature and sea-ice effective ice thickness were accessed via the website http://apdrc.soest.hawaii.edu/datadoc/ecco2_cube92.php (accessed on 9 May 2024). The ITS_LIVE ice velocity product was accessed via the website https://nsidc.org/apps/itslive/ (accessed on 9 May 2024). The index Kp, index AU&AL, and SYM-H were accessed via the website https://www.sws.bom.gov.au/ (accessed on 9 May 2024). The grounding line data was accessed via the website https://nsidc.org/data/nsidc-0593 (accessed on 9 May 2024).

Acknowledgments: We thank the ESA and ASF for providing Sentinel-1 SAR images and NASA for providing MODIS images. We thank the National Snow & Ice Data Center (NSIDC) for publishing the ITS_LIVE ice velocity and the grounding line data. We also thank the Australian Space Weather Forecasting Center (ASWFC) for offsetting the geomagnetic index Kp, auroral current aggregation index AU&AL, and geomagnetic symmetric disturbance component SYM-H.

Conflicts of Interest: The authors declare no conflict of interest.

References

1. Shen, Q.; Wang, H.; Shum, C.K.; Jiang, L.; Hsu, H.T.; Dong, J. Recent high-resolution Antarctic ice velocity maps reveal increased mass loss in Wilkes Land, East Antarctica. *Sci. Rep.* **2018**, *8*, 4477. [CrossRef] [PubMed]
2. Gardner, A.S.; Moholdt, G.; Scambos, T.; Fahnstock, M.; Ligtenberg, S.; van den Broeke, M.; Nilsson, J. Increased West Antarctic and unchanged East Antarctic ice discharge over the last 7 years. *Cryosphere* **2018**, *12*, 521–547. [CrossRef]
3. Völz, V.; Hinkel, J. Sea Level Rise Learning Scenarios for Adaptive Decision-Making Based on IPCC AR6. *Earth's Future* **2023**, *11*, e2023EF003662. [CrossRef]
4. Aoki, S.; Takahashi, T.; Yamazaki, K.; Hirano, D.; Ono, K.; Kusahara, K.; Tamura, T.; Williams, G.D. Warm surface waters increase Antarctic ice shelf melt and delay dense water formation. *Commun. Earth Environ.* **2022**, *3*, 142–150. [CrossRef]
5. Jacobs, S.; Giulivi, C.; Dutrieux, P.; Rignot, E.; Nitsche, F.; Mouginot, J. Getz Ice Shelf melting response to changes in ocean forcing. *J. Geophys. Res. Ocean.* **2013**, *118*, 4152–4168. [CrossRef]
6. Lei, Y.; Gardner, A.; Agram, P. Autonomous Repeat Image Feature Tracking (autoRIFT) and Its Application for Tracking Ice Displacement. *Remote Sens.* **2021**, *13*, 749. [CrossRef]
7. Shen, Q.; Wang, H.; Shum, C.K.; Jiang, L.; Hsu, H.; Gao, F.; Zhao, Y. Antarctic-wide annual ice flow maps from Landsat 8 imagery between 2013 and 2019. *Int. J. Digit. Earth* **2020**, *14*, 597–618. [CrossRef]
8. Dirscherl, M.; Dietz, A.J.; Dech, S.; Kuenzer, C. Remote sensing of ice motion in Antarctica—A review. *Remote Sens. Environ.* **2020**, *237*, 111595. [CrossRef]
9. Joughin, I.; Smith, B.E.; Abdalati, W. Glaciological advances made with interferometric synthetic aperture radar. *J. Glaciol.* **2017**, *56*, 1026–1042. [CrossRef]
10. Nagler, T.; Rott, H.; Hetzenecker, M.; Wuite, J.; Potin, P. The Sentinel-1 Mission: New Opportunities for Ice Sheet Observations. *Remote Sens.* **2015**, *7*, 9371–9389. [CrossRef]
11. Wang, X.; Holland, D.M. An Automatic Method for Black Margin Elimination of Sentinel-1A Images over Antarctica. *Remote Sens.* **2020**, *12*, 1175. [CrossRef]
12. Mouginot, J.; Scheuchl, B.; Rignot, E. Mapping of Ice Motion in Antarctica Using Synthetic-Aperture Radar Data. *Remote Sens.* **2012**, *4*, 2753–2767. [CrossRef]
13. Rignot, E.; Mouginot, J.; Scheuchl, B.; Jeong, S. Changes in Antarctic Ice Sheet Motion Derived From Satellite Radar Interferometry Between 1995 and 2022. *Geophys. Res. Lett.* **2022**, *49*, e2022GL100141. [CrossRef]
14. Jawak, S.D.; Kumar, S.; Luis, A.J.; Pandit, P.H.; Wankhede, S.F.; Anirudh, T.S. Seasonal Comparison of Velocity of the Eastern Tributary Glaciers, Amery Ice Shelf, Antarctica, Using Sar Offset Tracking. *ISPRS Ann. Photogramm. Remote Sens. Spat. Inf. Sci.* 2019; IV-2/W5, 595–600. [CrossRef]
15. Schubert, A.; Faes, A.; Kääb, A.; Meier, E. Glacier surface velocity estimation using repeat TerraSAR-X images: Wavelet- vs. correlation-based image matching. *ISPRS J. Photogramm. Remote Sens.* **2013**, *82*, 49–62. [CrossRef]
16. Fanghui, D.; Chunxia, Z.; Zemin, W.; Chen, D.; Xin, Z. Ice-flow Velocity Derivation of the Confluence Zone of the Amery Ice Shelf Using Offset-tracking Method. *Geomat. Inf. Sci. Wuhan Univ.* **2015**, *40*, 901–908.
17. Manson, R.; Coleman, R.; Morgan, P.; King, M. Ice velocities of the Lambert Glacier from static GPS observations. *Earth Planets Space* **2000**, *52*, 6. [CrossRef]
18. Zhou, C.; Liang, Q.; Chen, Y.; Lei, H.; Fu, Z.; Zheng, L.; Liu, R. Mass Balance Assessment of the Amery Ice Shelf Basin, East Antarctica. *Earth Space Sci.* **2019**, *6*, 1987–1999. [CrossRef]
19. Tong, X.; Liu, S.; Li, R.; Xie, H.; Liu, S.; Qiao, G.; Feng, T.; Tian, Y.; Ye, Z. Multi-track extraction of two-dimensional surface velocity by the combined use of differential and multiple-aperture InSAR in the Amery Ice Shelf, East Antarctica. *Remote Sens. Environ.* **2018**, *204*, 122–137. [CrossRef]
20. Chi, Z.; Klein, A.G. Inter- and Intra-annual Surface Velocity Variations at the Southern Grounding Line of Amery Ice Shelf from 2014 to 2018. *Cryosphere Discuss.* 2020; *preprint*. [CrossRef]
21. Liang, Q.I.; Zhou, C.; Howat, I.M.; Jeong, S.; Liu, R.; Chen, Y. Ice flow variations at Polar Record Glacier, East Antarctica. *J. Glaciol.* **2019**, *65*, 279–287. [CrossRef]
22. Zhou, C.; Zhou, Y.; Deng, F.; Ai, S.; Wang, Z.; E, D. Seasonal and interannual ice velocity changes of Polar Record Glacier, East Antarctica. *Ann. Glaciol.* **2017**, *55*, 45–51. [CrossRef]
23. Walker, C.C.; Becker, M.K.; Fricker, H.A. A High Resolution, Three-Dimensional View of the D-28 Calving Event From Amery Ice Shelf With ICESat-2 and Satellite Imagery. *Geophys. Res. Lett.* **2021**, *48*, e2020GL091200. [CrossRef]
24. Galton-Fenzi, B.K.; Hunter, J.R.; Coleman, R.; Marsland, S.J.; Warner, R.C. Modeling the basal melting and marine ice accretion of the Amery Ice Shelf. *J. Geophys. Res. Ocean.* **2012**, *117*, C09031. [CrossRef]

25. Lei, Y.; Gardner, A.S.; Agram, P. Processing methodology for the ITS_LIVE Sentinel-1 ice velocity products. *Earth Syst. Sci. Data* **2022**, *14*, 5111–5137. [CrossRef]
26. Mouginot, J.; Rignot, E.; Scheuchl, B. Continent-Wide, Interferometric SAR Phase, Mapping of Antarctic Ice Velocity. *Geophys. Res. Lett.* **2019**, *46*, 9710–9718. [CrossRef]
27. Li, B.; Wang, Z.; An, J.; Zhang, B.; Geng, H.; Ma, Y.; Li, M.; Qian, Y. Ionospheric Phase Compensation for InSAR Measurements Based on the Faraday Rotation Inversion Method. *Sensors* **2020**, *20*, 6877. [CrossRef]
28. Liao, H.; Meyer, F.J.; Scheuchl, B.; Mouginot, J.; Joughin, I.; Rignot, E. Ionospheric correction of InSAR data for accurate ice velocity measurement at polar regions. *Remote Sens. Environ.* **2018**, *209*, 166–180. [CrossRef]
29. Liang, C.; Agram, P.; Simons, M.; Fielding, E.J. Ionospheric Correction of InSAR Time Series Analysis of C-band Sentinel-1 TOPS Data. *IEEE Trans. Geosci. Remote Sens.* **2019**, *57*, 6755–6773. [CrossRef]
30. Kamel Hasni, J.C.; Wei, G. Correcting Ionospheric and Orbital Errors in Spaceborne SAR Differential Interferograms. In Proceedings of the 2017 IEEE International Conference on Imaging Systems and Techniques (IST), Beijing, China, 18–20 October 2017.
31. Ma, Y.; Wang, Z.; Li, F.; Liu, S.; An, J.; Li, B.; Ma, W. Ionospheric Correction of L-Band SAR Interferometry for Accurate Ice-Motion Measurements: A Case Study in the Grove Mountains Area, East Antarctica. *Remote Sens.* **2022**, *14*, 556. [CrossRef]
32. Kumar, V.V.; Parkinson, M.L. A global scale picture of ionospheric peak electron density changes during geomagnetic storms. *Space Weather* **2017**, *15*, 637–652. [CrossRef]
33. Consortium, E.; Fukumori, I.; Wang, O.; Fenty, I.; Forget, G.; Heimbach, P.; Ponte, R. Synopsis of the ECCO Central Production Global Ocean and Sea-Ice State Estimate, Version 4 Release 4, Zenodo [Data Set]. 2021. Available online: https://openpolar.no/Record/ftdatacite:10.5281/zenodo.3765928 (accessed on 9 May 2024).
34. Fukumori, I.; Fenty, I.G.; Forget, G.; Heimbach, P.; King, C.; Nguyen, A.T.; Piecuch, C.G.; Ponte, R.M.; Vinogradov, N.; Wang, O. Data sets used in ECCO Version 4 Release 3. 2019. Available online: https://dspace.mit.edu/handle/1721.1/120472 (accessed on 9 May 2024).
35. Zhao, J.; Cheng, B.; Vihma, T.; Heil, P.; Hui, F.; Shu, Q.; Zhang, L.; Yang, Q. Fast Ice Prediction System (FIPS) for land-fast sea ice at Prydz Bay, East Antarctica: An operational service for CHINARE. *Ann. Glaciol.* **2020**, *61*, 271–283. [CrossRef]
36. Gomez-Fell, R.; Rack, W.; Purdie, H.; Marsh, O. Parker Ice Tongue Collapse, Antarctica, Triggered by Loss of Stabilizing Land-Fast Sea Ice. *Geophys. Res. Lett.* **2022**, *49*, e2021GL096156. [CrossRef]
37. Li, X.; Shokr, M.; Hui, F.; Chi, Z.; Heil, P.; Chen, Z.; Yu, Y.; Zhai, M.; Cheng, X. The spatio-temporal patterns of landfast ice in Antarctica during 2006–2011 and 2016–2017 using high-resolution SAR imagery. *Remote Sens. Environ.* **2020**, *242*, 111736. [CrossRef]
38. Hoppmann, M.; Nicolaus, M.; Hunkeler, P.A.; Heil, P.; Behrens, L.K.; König-Langlo, G.; Gerdes, R. Seasonal evolution of an ice-shelf influenced fast-ice regime, derived from an autonomous thermistor chain. *J. Geophys. Res. Ocean.* **2015**, *120*, 1703–1724. [CrossRef]
39. Mallett, R.D.C.; Stroeve, J.C.; Tsamados, M.; Landy, J.C.; Willatt, R.; Nandan, V.; Liston, G.E. Faster decline and higher variability in the sea ice thickness of the marginal Arctic seas when accounting for dynamic snow cover. *Cryosphere* **2021**, *15*, 2429–2450. [CrossRef]
40. Xu, Y.; Li, H.; Liu, B.; Xie, H.; Ozsoy-Cicek, B. Deriving Antarctic Sea-Ice Thickness From Satellite Altimetry and Estimating Consistency for NASA's ICESat/ICESat-2 Missions. *Geophys. Res. Lett.* **2021**, *48*, e2021GL0934250. [CrossRef]
41. Zhang, B.; Wang, Z.; An, J.; Yan, B.; Liu, M.; Wu, S. *Antarctic Ice Shelves Surface Elevation, Thickness and Basal Mass Balance (1991–2020)*; National Tibetan Plateau/Third Pole Environment Data Center: Beijing, China, 2023. [CrossRef]
42. Nitsche, F.O.; Gohl, K.; Larter, R.D.; Hillenbrand, C.D.; Kuhn, G.; Smith, J.A.; Jacobs, S.; Anderson, J.B.; Jakobsson, M. Paleo ice flow and subglacial meltwater dynamics in Pine Island Bay, West Antarctica. *Cryosphere* **2013**, *7*, 249–262. [CrossRef]
43. Herraiz-Borreguero, L.; Church, J.A.; Allison, I.; Peña-Molino, B.; Coleman, R.; Tomczak, M.; Craven, M. Basal melt, seasonal water mass transformation, ocean current variability, and deep convection processes along the Amery Ice Shelf calving front, East Antarctica. *J. Geophys. Res. Ocean.* **2016**, *121*, 4946–4965. [CrossRef]
44. Lee, S.; Kim, S.; An, H.; Han, H. Ice Velocity Variations of the Cook Ice Shelf, East Antarctica, from 2017 to 2022 from Sentinel-1 SAR Time-Series Offset Tracking. *Remote Sens.* **2023**, *15*, 3079. [CrossRef]
45. Han, H.; Im, J.; Kim, H.-c. Variations in ice velocities of Pine Island Glacier Ice Shelf evaluated using multispectral image matching of Landsat time series data. *Remote Sens. Environ.* **2016**, *186*, 358–371. [CrossRef]
46. Scambos, T.A.; Bohlander, J.A.; Shuman, C.A.; Skvarca, P. Glacier acceleration and thinning after ice shelf collapse in the Larsen B embayment, Antarctica. *Geophys. Res. Lett.* **2004**, *31*, L18402. [CrossRef]
47. Herraiz-Borreguero, L.; Coleman, R.; Allison, I.; Rintoul, S.R.; Craven, M.; Williams, G.D. Circulation of modified Circumpolar Deep Water and basal melt beneath the Amery Ice Shelf, East Antarctica. *J. Geophys. Res. Ocean.* **2015**, *120*, 3098–3112. [CrossRef]
48. Liu, C.; Wang, Z.; Cheng, C.; Wu, Y.; Xia, R.; Li, B.; Li, X. On the Modified Circumpolar Deep Water Upwelling Over the Four Ladies Bank in Prydz Bay, East Antarctica. *J. Geophys. Res. Ocean.* **2018**, *123*, 7819–7838. [CrossRef]
49. Liu, C.; Wang, Z.; Cheng, C.; Xia, R.; Li, B.; Xie, Z. Modeling modified Circumpolar Deep Water intrusions onto the Prydz Bay continental shelf, East Antarctica. *J. Geophys. Res. Ocean.* **2017**, *122*, 5198–5217. [CrossRef]

50. Wang, T.; Zhou, C.; Qian, Y.; Chen, G.; Zhu, D.; Zhu, Y.; Liu, Y. Basal Channel System and Polynya Effect on a Regional Air-Ice-Ocean-Biology Environment System in the Prydz Bay, East Antarctica. *J. Geophys. Res. Earth Surf.* **2023**, *128*, e2023JF007286. [CrossRef]
51. Davies, B.J.; Carrivick, J.L.; Glasser, N.F.; Hambrey, M.J.; Smellie, J.L. Variable glacier response to atmospheric warming, northern Antarctic Peninsula, 1988–2009. *Cryosphere* **2012**, *6*, 1031–1048. [CrossRef]
52. Francis, D.; Mattingly, K.S.; Lhermitte, S.; Temimi, M.; Heil, P. Atmospheric extremes triggered the biggest calving event in more than 50 years at the Amery Ice shelf in September 2019. *Cryosphere* **2021**, *15*, 2147–2165. [CrossRef]
53. Gudmundsson, G.H. Ice-shelf buttressing and the stability of marine ice sheets. *Cryosphere* **2013**, *7*, 647–655. [CrossRef]
54. Li, T.; Liu, Y.; Cheng, X. Recent and imminent calving events do little to impair Amery ice shelf's stability. *Acta Oceanol. Sin.* **2020**, *39*, 168–170. [CrossRef]
55. Fürst, J.J.; Durand, G.; Gillet-Chaulet, F.; Tavard, L.; Rankl, M.; Braun, M.; Gagliardini, O. The safety band of Antarctic ice shelves. *Nat. Clim. Chang.* **2016**, *6*, 479–482. [CrossRef]